

Article

Three-Dimensional Numerical Investigation of the Asymmetric Discard Characteristics of Hypervelocity Projectile Sabot

Xuefeng Yang , Junyong Lu *, Bai Li, Sai Tan and Zhiqiang Xie

National Key Laboratory of Electromagnetic Energy, Naval University of Engineering, Wuhan 430033, China

* Correspondence: 0910061051@nue.edu.cn

Abstract: Sabots are vital to the successful launch of hypervelocity projectiles (HVPs), supporting and protecting the projectile's flight body within the barrel. After the projectile exits the muzzle, aerodynamic forces induce relative motion between the sabot and the flight body, termed 'sabot discard'. During this process, there are complex aerodynamic interactions between the sabot and flight body. These interactions impact the flight body's flight stability and accuracy. This research focuses on an HVP with a two-segment sabot at Mach 7.2, employing the unstructured overset grid method and three-degree-of-freedom model to investigate the impact of the angle of attack (AOA) on the discard. At the AOA = 0 Deg, the sabot segments' movement is symmetric, causing fluctuations in the flight body's drag. However, at AOAs \neq 0 Deg, the sabot segments' movement becomes asymmetric. The upper sabot segment accelerates while the lower one decelerates, causing significant fluctuations in drag and lift, and prolonged disturbance. As the AOA increases, both asymmetry and disturbances intensify. Notably, at the AOA = 8 Deg, the absolute value of the discard angle difference between the upper and lower sabot segments reaches 45 Deg. Considering the AOA's impact, it is advisable to maintain the AOA for HVP sabot discard in the range of $[-2, 2]$ Deg.

Keywords: asymmetric discard; hypervelocity projectile; overset grid; shock wave; three-degree-of-freedom model



Academic Editor: Sergey Leonov

Received: 21 January 2025

Revised: 19 February 2025

Accepted: 23 February 2025

Published: 26 February 2025

Citation: Yang, X.; Lu, J.; Li, B.; Tan, S.; Xie, Z. Three-Dimensional Numerical Investigation of the Asymmetric Discard Characteristics of Hypervelocity Projectile Sabot.

Aerospace **2025**, *12*, 187. <https://doi.org/10.3390/aerospace12030187>

Copyright: © 2025 by the authors. Licensee MDPI, Basel, Switzerland. This article is an open access article distributed under the terms and conditions of the Creative Commons Attribution (CC BY) license (<https://creativecommons.org/licenses/by/4.0/>).

1. Introduction

Research on hypervelocity projectiles (HVPs) and associated launch technologies has become a significant area of focus within numerous institutions [1]. Currently, a variety of launch technologies are capable of attaining hypervelocity performance. These technologies encompass single-stage gas guns (SSGs), single-stage powder guns (SSPGs), two-stage light gas guns (2SLGGs), three-stage light gas guns (3SLGGs), Van de Graaff accelerators (VDFs), laser-driven flyers (LDFs), laser-induced particle impact tests (LIPTs), rocket sleds, railguns, and plasma guns, among others [1,2]. HVPs are generally sub-caliber and usually consist of the flight body and the sabot [3,4]. In the launch tube, the sabot and the flight body are accelerated together from rest to hypervelocity. In the field of hypervelocity impact, this combination of the projectile body and the sabot is also referred to as the 'projectile package' or 'launch package' [5,6]. The sabot mainly functions to support and protect the flight body, while reducing undesired lateral or yawing motions [7,8]. After the HVPs exit the muzzle, the sabot separates from the flight body, and this process is called 'sabot discard'. Techniques for sabot discard involve utilizing aerodynamic forces, mechanical devices, tangential forces, and other methods. The most prevalent technique for achieving sabot discard is through the use of aerodynamic force [7]. This method operates on the principle that varying aerodynamic loads on the sabot

and the flight body create a relative motion between the two. However, during this type of sabot discard relying on aerodynamic forces, there is complex aerodynamic interference between the flight body and the sabot. This complex aerodynamic interference will affect the flight body's subsequent flight stability and shooting accuracy [9]. Consequently, it is essential to study the aerodynamics involved in sabot discard for HVPs. Furthermore, to eliminate any potential ambiguity, all mentions of sabot discard in the following parts of this paper specifically refer to the method achieved by aerodynamic forces.

Sabot discard is typical multi-body dynamics in the aerospace field [10], which is characterized in a similar way to store separation [11], multi-stage vehicle separation [12], and shroud deployment [13]. The defining feature of multi-body dynamics is that there are no direct mutual constraints or contacts among the multi-bodies (specifically, the sabot and the flight body), but only air–medium interactions. An interaction flow field interference effect exists among the multi-bodies throughout the discard. The flow field interference can significantly impact the multi-body aerodynamic characteristics, which in turn influence their motion characteristics, while the motion characteristics also affect the flow field. Therefore, the aerodynamic and motion characteristics are interdependent and exhibit a coupling effect [14]. The methodologies employed in multi-body dynamics mainly include engineering test methods and numerical simulation methods.

In the early stage, the study on sabot discard generally adopted the method of engineering experiments. Schmidt [15] evaluated the surface pressures of the sabot and the flight body at Mach 4.5 through wind tunnel tests. The experimental results pointed out that the impact of shock waves on the surface of the flight body led to the appearance of local pressure peaks on the surface of the flight body. Li et al. [16] adopted the display and measurement method of the Fresnel lens indirect shadow to obtain photos of the sabot discard of the fin-stabilized discarding sabot armor-piercing projectile (APFSDS) near the muzzle area. Moreover, they analyzed and evaluated the forces and movements based on the measurement results. Zielinski et al. [17] evaluated factors causing the delayed discard of the sabot by analyzing its movement in the launch tests.

Experiments are also limited by current in situ diagnostic capabilities. Therefore, it is of great significance to use numerical methods to solve and simulate the sabot discard [10]. Huang et al. [18] calculated and analyzed the sabot discard of the APFSDS at Mach 4 by coupling and solving the Euler equations and the six-degree-of-freedom (6DOF) equations based on dynamic grid technology. They also analyzed the discard trajectory of the sabot relative to the flight body and the variations in the aerodynamic parameters of the flight body. Li et al. [19] established a sabot discard model adopting dynamic grid technology. They analyzed the changes in the aerodynamic parameters of the sabot and the flight body during the discard under different incoming flow Mach numbers. Reck et al. [20] established an inviscid sabot discard model at Mach 4.5 using Autodyn software, and they calculated and solved the sabot discard near the muzzle. Based on the model, the muzzle disturbance was also analyzed. Mohanan et al. [21] calculated and evaluated the discard trajectories and aerodynamic forces of different sabot designs during the discard at Mach 3 by coupling the one-dimensional compressible flow equations and the three-degree-of-freedom (3DOF) equations. Kasahara et al. [22] analyzed the shock wave interaction between the flight body and the sabot and the changes in the unsteady aerodynamic loads acting on the flight body during the sabot discard when the muzzle initial velocity reached 2501 m/s by coupling and solving the Euler equations and the 6DOF equations based on the unstructured overset grid method. Kharlamov et al. [23] combined the launch experiment, used the Menter–SST $k - \omega$ turbulence model to solve the steady N–S equations, and calculated and analyzed the impact of different angles of sabot discard on the flight body.

They also explained and supported the experimental phenomena. The results provided a reference for the subsequent optimized design of the sabot.

In summary, previous studies mainly focused on scenarios below Mach 5. However, the speed of HVP far exceeds Mach 5, and the sabot discard flow field is more complex [22]. Furthermore, most previous studies are based on assumptions that the angle of attack (AOA) is 0 Deg. Nevertheless, in actual launches, due to the deviation of the projectile's mass and center of mass, the variation in the clearance between the projectile and the gun barrel, the vibration of the launching platform, and the influence of environmental wind direction, it is unlikely for the projectile to be entirely at the AOA = 0 Deg after exiting the muzzle [24,25]. The non-zero AOA will cause the movement of the sabot relative to the flight body to be asymmetrical, termed 'asymmetric sabot discard', further increasing the aerodynamic disturbance on the flight body [26]. HVPs have a higher flight speed, and the asymmetric sabot discard caused by the non-zero AOA and the disturbance of this asymmetry on the flight body is more significant.

In this paper, the Realizable $k - \varepsilon$ turbulence model and the 3DOF motion model are adopted. For HVP at Mach 7.2 with upper and lower sabot segments, numerical calculations are conducted to examine the influence of the AOA on sabot discard. The characteristics of symmetric and asymmetric sabot discard flow fields are obtained. The research results may contribute to a deeper understanding of sabot discard and serve as a valuable reference for suppressing AOA disturbances.

2. Methods

2.1. Research Object

Taking the three-dimensional model of the HVP cited in Reference [22] as the research object, this projectile consists of three components: the upper sabot segment, the lower sabot segment, and the flight body. The flight body has a conical structure with a spherical nose. The sabot has a special-shaped structure, with the upper and lower sabot segments being mirror-symmetric. This projectile is accelerated from rest to 2501 m/s, approximately Mach 7.2, within 2.19 ms by electromagnetic forces [22]. The detailed geometric parameters of the projectile are not disclosed in Reference [22]. The modified model made in the current work and the detailed geometry are shown in Figure 1.

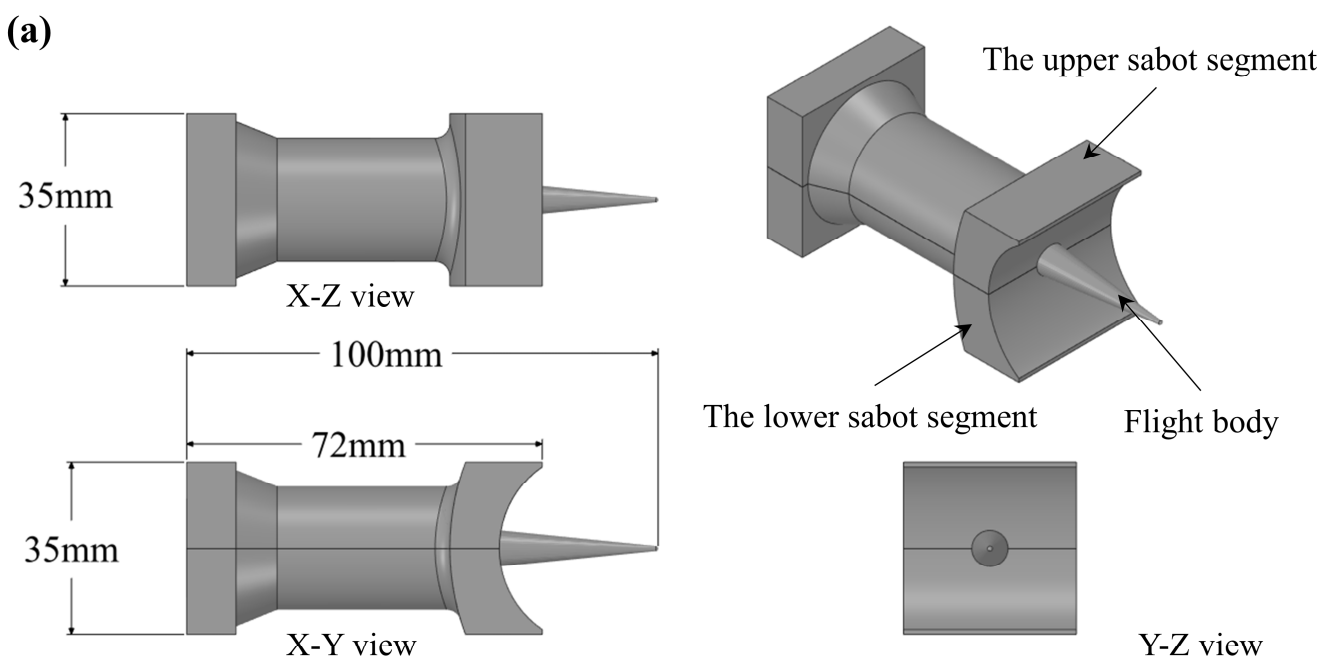


Figure 1. Cont.

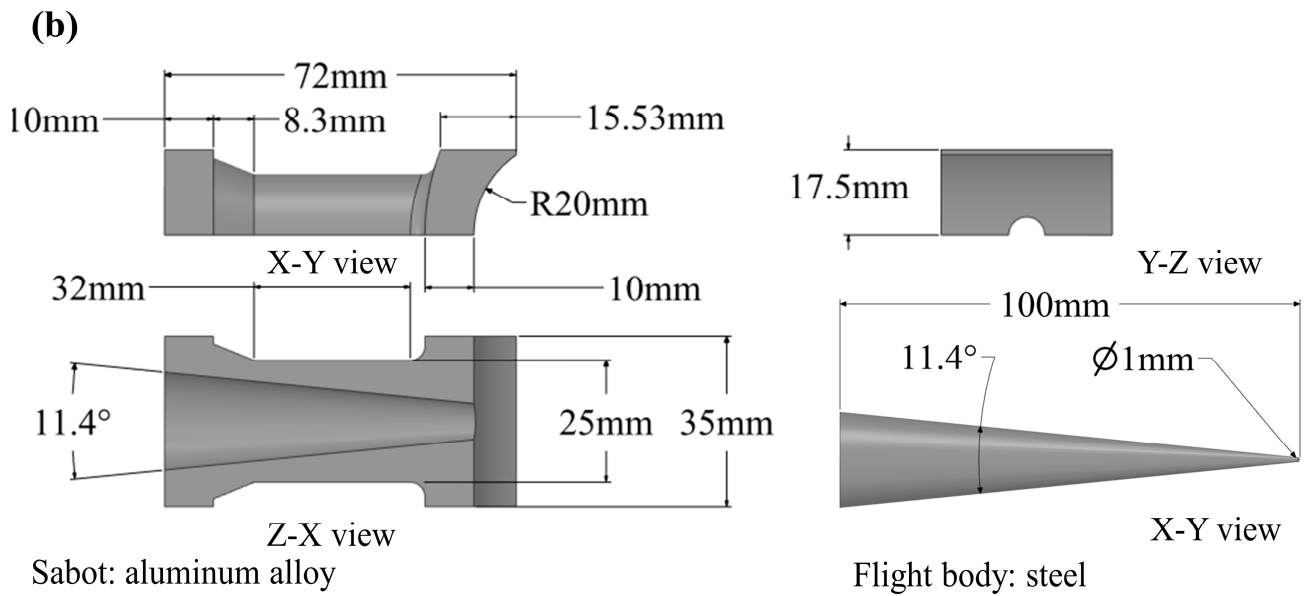


Figure 1. Schematic of the HVP, adapted from reference [22]: (a) HVP; and (b) the sabot and the flight body.

2.2. Governing Equations

The airflow around the projectile is in a three-dimensional, transient viscous turbulent state and obeys the governing equations [27]:

$$\frac{\partial(\rho\phi)}{\partial t} + \text{div}[\rho(u - u_g)\phi] = \text{div}(\Gamma \text{grad } \phi) + S \tag{1}$$

where t , u , u_g , ϕ , Γ , and S are the time, velocity vector of the airflow, migration velocity, flow field flux, diffusion coefficient, and source item, respectively. The turbulence model is significant for the simulation. The Realizable $k - \epsilon$ turbulence model is adopted in this paper. For a comprehensive and detailed description of the turbulent kinetic energy k and turbulent dissipation rate ϵ of the turbulence model, refer to Reference [28].

In launch tests, high aerodynamic forces can lead to the deformation of the sabot, thereby impacting its aerodynamic properties [29]. This study primarily examines the characteristics of the sabot discard flow field, with particular emphasis on the effects of the AOA on this discard process. It is important to note that accounting for wall deformation in computational fluid dynamics (CFDs) entails considerable computational expense. Consequently, the numerical method employed in this research adopts a rigid-body assumption, thereby disregarding the aeroelasticity or deformation of moving objects [30].

Disregarding aeroelasticity, an object’s motion can be simplified to the translational movement of its center of mass and the rotational movement about that center of mass, obeying 6DOF motion equations [30]:

$$\begin{bmatrix} \dot{u}_s \\ \dot{v}_s \\ \dot{w}_s \end{bmatrix} = \begin{bmatrix} \frac{F_x}{m} \\ \frac{F_y}{m} \\ \frac{F_z}{m} \end{bmatrix} = \begin{bmatrix} 0 & -r & q \\ r & 0 & -p \\ -q & p & 0 \end{bmatrix} \begin{bmatrix} u_s \\ v_s \\ w_s \end{bmatrix} \tag{2}$$

$$\begin{bmatrix} \dot{p} \\ \dot{q} \\ \dot{r} \end{bmatrix} = I^{-1} \left\{ \begin{bmatrix} M_x \\ M_y \\ M_z \end{bmatrix} - \begin{bmatrix} 0 & -r & q \\ r & 0 & -p \\ -q & p & 0 \end{bmatrix} [I] \begin{bmatrix} p \\ q \\ r \end{bmatrix} \right\} \tag{3}$$

where, (u_s, v_s, w_s) are the velocities of the center of mass in the body reference frame, (p, q, r) are the angular velocities in the body reference frame, (F_x, F_y, F_z) and

(M_x, M_y, M_z) are the aerodynamic forces and moments, respectively, and I is the rotational inertia tensor.

In this paper, a half model is adopted, considering the model's symmetry. Therefore, parameters such as $\dot{w}_s, w_s, \dot{p}, \dot{q}, p, q, F_z, M_x,$ and M_y can be ignored, and the 6DOF motion equations are simplified into 3DOF motion equations:

$$\begin{bmatrix} \dot{u}_s \\ \dot{v}_s \\ \dot{r} \end{bmatrix} = \begin{bmatrix} \frac{F_x}{m} \\ \frac{F_y}{m} \\ \frac{M_z}{I_{zz}} \end{bmatrix} = \begin{bmatrix} 0 & -r & 0 \\ r & 0 & 0 \\ 0 & 0 & 0 \end{bmatrix} \begin{bmatrix} u_s \\ v_s \\ 0 \end{bmatrix} \quad (4)$$

The process of coupling and resolving the N-S equations and the 3DOF motion equations is outlined as follows [31]:

- Step 1: The aerodynamic forces and moments at the current moment are obtained by solving the N-S equations;
- Step 2: Based on the forces and moments, the acceleration and angular acceleration of the sabot at the current moment are obtained by solving the 3DOF equations;
- Step 3: The displacement and pitch angle of the sabot at the next moment can be obtained through numerical integration;
- Step 4: Repeat the Step 1, 2, and 3 until the calculation stops.

2.3. Calculation Grid

Given that the overset mesh method is relatively mature for simulating unsteady flows with relative motion [32,33], it is adopted to simulate the process of sabot discard in this paper.

The half-model is used in this study to improve calculation efficiency. According to the composition of the model, the grid is divided into three parts: the background grid containing the flight body, the sub-grid containing the upper sabot segment, and the other sub-grid containing the lower sabot segment. The polyhedral meshing method is used to mesh the model, and local refinement is carried out. By controlling the height of the first layer of wall grids, the y^+ is ensured to be from 30 to 300. The meshed grids are shown in Figures 2 and 3.

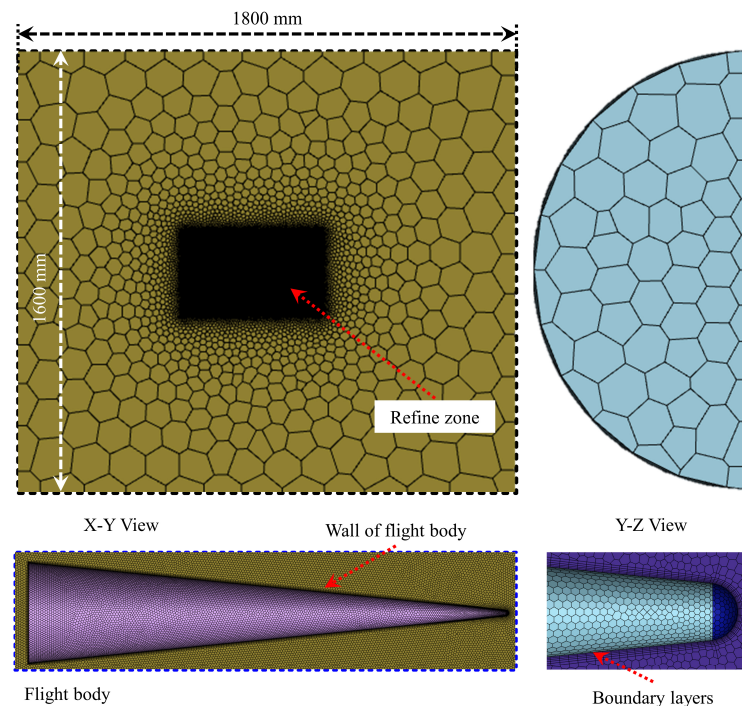


Figure 2. Schematic of the background grid.

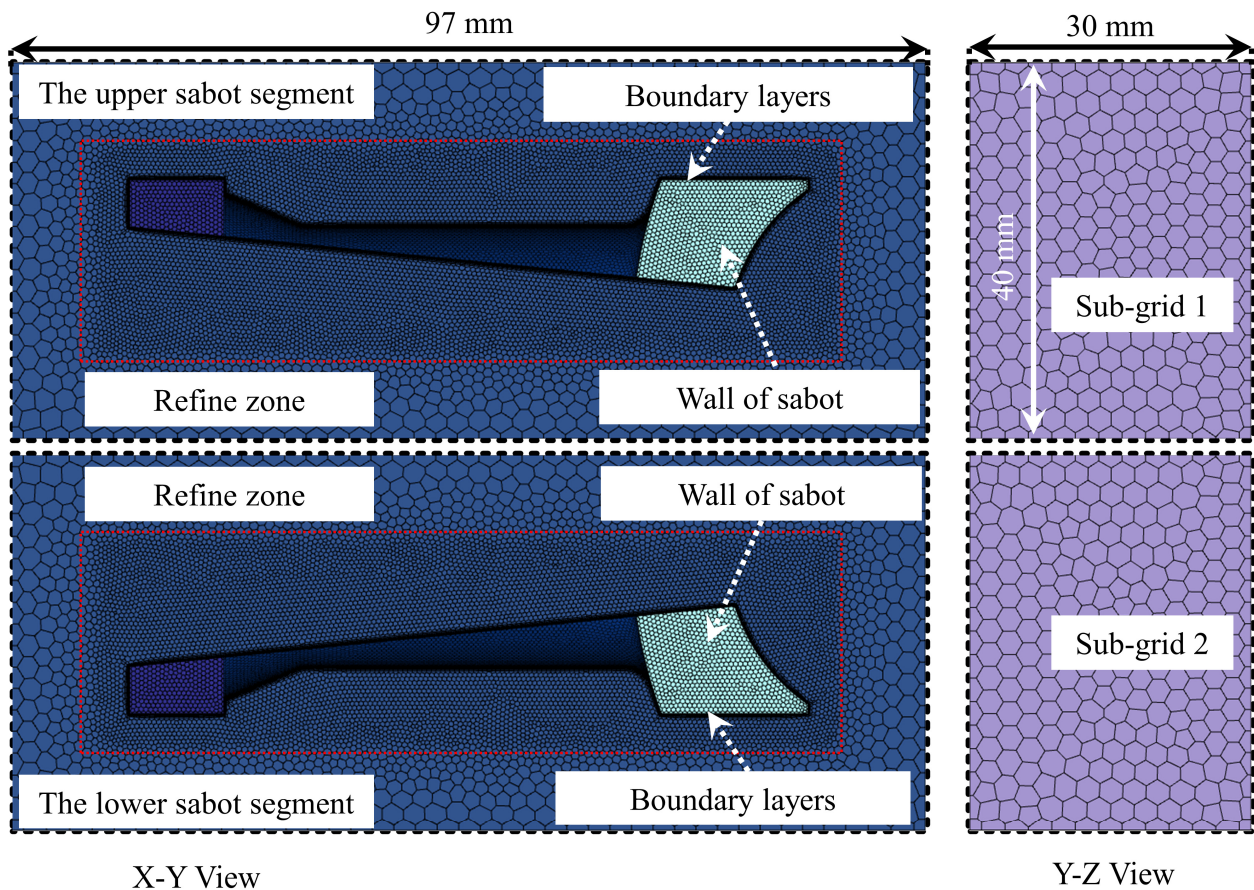


Figure 3. Schematic of the sub-grids.

Figure 2 shows the background grid. The background grid contains the flight body. The background grid area is a cylinder with a length of 1800 mm and a radius of 800 mm. Considering the movement of the sabot, local refinement is carried out in the areas involved in the movement of the upper and lower sabot segments in the background grid. The number of polyhedral grid elements in the background grid is about 1 million, the minimum grid size is 0.05 mm, and the maximum is 150 mm. The sub-grids contain the sabot segments, and the sub-grid area is a cuboid with a length of 97 mm, a width of 40 mm, and a height of 30 mm, as shown in Figure 3. Local refinement is carried out on the grids near the wall surfaces of the sabot. Sub-grids are symmetric about the X–Z plane. The number of polyhedral grid elements in one sub-grid is about 0.2 million, the minimum grid size is 0.05 mm, and the maximum is 4 mm.

2.4. Assumptions and Boundary Conditions

Considering that the HVP's flight altitude is relatively low during sabot discard, the ambient static pressure and static temperature selected in this study are 101,325 Pa and 300 K, respectively [20].

The X–Y plane of the background grid is a symmetric boundary condition. The remaining outer boundaries are pressure far-field conditions, with the incoming flow Mach 7.2. The X–Y plane of the two sub-grids are symmetric boundary conditions, and the remaining outer boundaries are overset boundary conditions. The walls of the flight body and the sabot in both the background grid and the sub-grids are no-slip adiabatic walls.

There are four typical cases designed in this study, as shown in Table 1. Case 1 and Case 2 are steady, while Case 3 and Case 4 are unsteady. In Case 1, the aerodynamic parameters of the flight body, including the drag and lift coefficients, are obtained. These aerodynamic

parameters are selected as the benchmark to analyze the disturbance from the sabot discard. In Case 3 and Case 4, the aerodynamic parameters of the flight body will change compared with the benchmark due to the sabot discard. These changed aerodynamic parameters will cause variations in the position and attitude angles of the flight body, which, in turn, will influence the aerodynamic parameters. This paper focuses on the influence of the disturbance brought by the sabot discard. By introducing the flight body's motion, the aerodynamic parameters are influenced by multiple factors, such as time-varying velocity and angular velocity. Therefore, to examine the impact of the disturbance resulting from the sabot discard and to enable a meaningful comparison with the benchmark, this study assumes that the flight body remains stationary during sabot discard.

Table 1. Calculation case.

	Object	AOA
Case 1	The steady flow field of the flight body	0–8 Deg
Case 2	The steady flow field of the HVP	0–8 Deg
Case 3	The unsteady flow field of the symmetric discard of the sabot	0 Deg
Case 4	The unsteady flow field of the asymmetric discard of the sabot	2–8 Deg

In addition, given that the duration of sabot discard is within milliseconds, the effect of gravity is negligible over such a brief interval. Therefore, gravity is disregarded in the calculations of the unsteady flow field.

The governing equations, unsteady N–S equations, are numerically solved based on the implicit method by using the finite volume method (FVM). The second-order upwind scheme is used for discretization in space, and the AUSM+ flux scheme is adopted. Gas is assumed to be ideal, which obeys the ideal gas law. The basic parameters of the flow field are shown in Table 2.

Table 2. Basic parameters of the flow field.

Parameters	Value
Reference density, ρ_r , [kg/m ³]	1.176674
Reference velocity, U_r , [m/s]	2501
Reference area, S_r , [m ²]	0.0001571
Reference length, L_r , [m]	0.1
Mass of the sabot, m , [kg]	0.0034
Moment of inertia of a sabot segment, I_{zz} , [kg·m ²]	2×10^{-5}
Mass center of the upper sabot segment [m]	3.0×10^{-2} , 1.0×10^{-2} , 0.0

3. Verification

3.1. Method Verification

The “wing-pylon-finned-store” (WPFS) multi-body separation standard model is adopted to verify the overset grid method used in this study, as shown in Figure 4. The wing has a semi-span of 6.6 m, the diameter of the store is 0.508 m, the length is 0.85 m, and the mass is 907.8 kg. The incoming flow velocity in the test is Mach 0.95, and the flight altitude is 8.0 km. More test details can be found in reference [34,35]. Figure 5 shows the test and calculation results. By referring to the numerical results in previous studies [36–39], the consistency of the calculation and test results presented in this paper validates the reliability of the method.

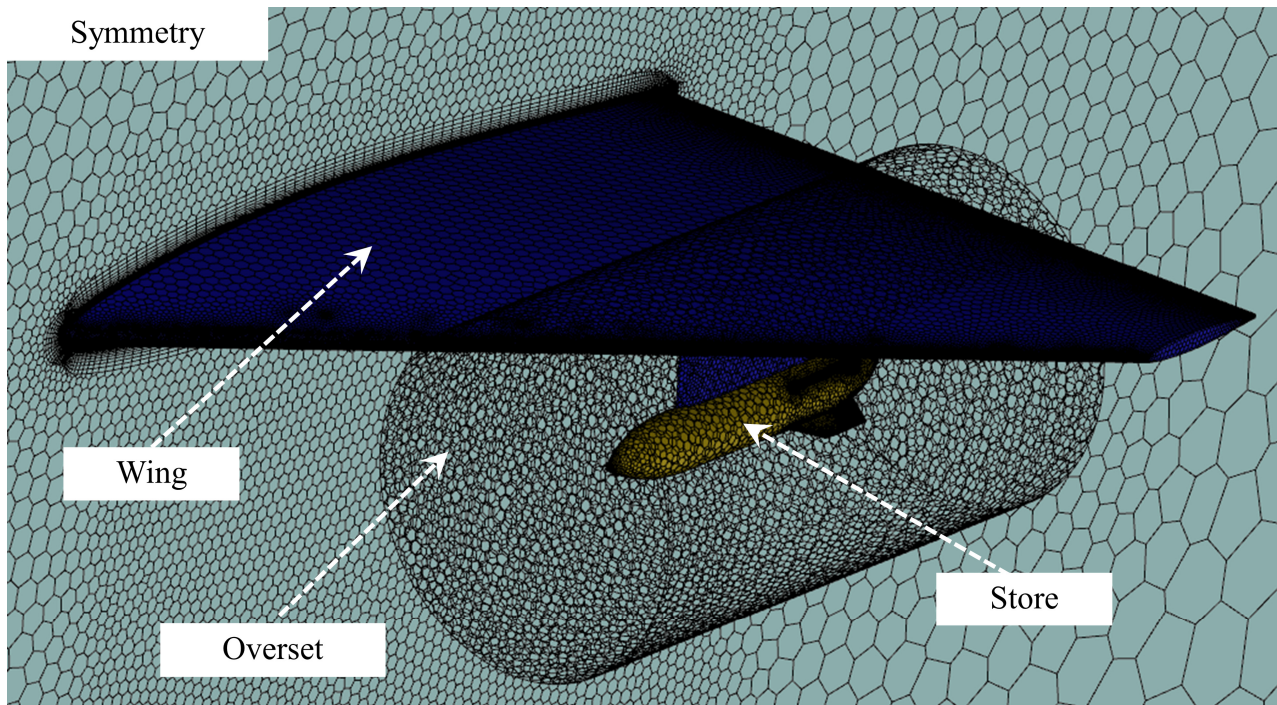


Figure 4. The model of the WPFS.

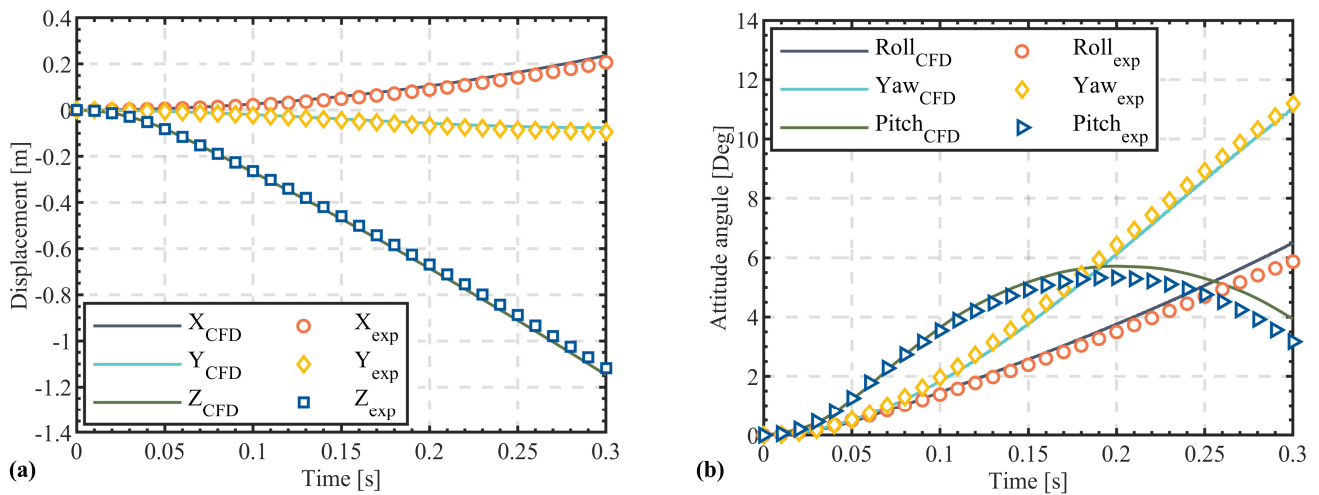


Figure 5. Comparison of experimental results and the calculation result: (a) displacement; and (b) attitude angle.

3.2. Grid Independence Verification

Three sets of grids with different numbers are meshed, 0.9 million, 1.4 million, and 1.92 million. At the AOA = 2 Deg, the axial force coefficients of the three grids are 0.06623, 0.06658, and 0.06634, respectively, with a 0.5% error. The normal force coefficients are 0.06632, 0.06615, and 0.06624, respectively, with a 0.3% error.

In the symmetric sabot discard, the sabot's displacements and discard angles are shown in Figure 6, and the three curves match very well. It is important to clarify that the term 'discard angle' is utilized to refer to the pitch angle. According to the results, it can be concluded that the medium grid selected in this study meets the requirements for grid independence.

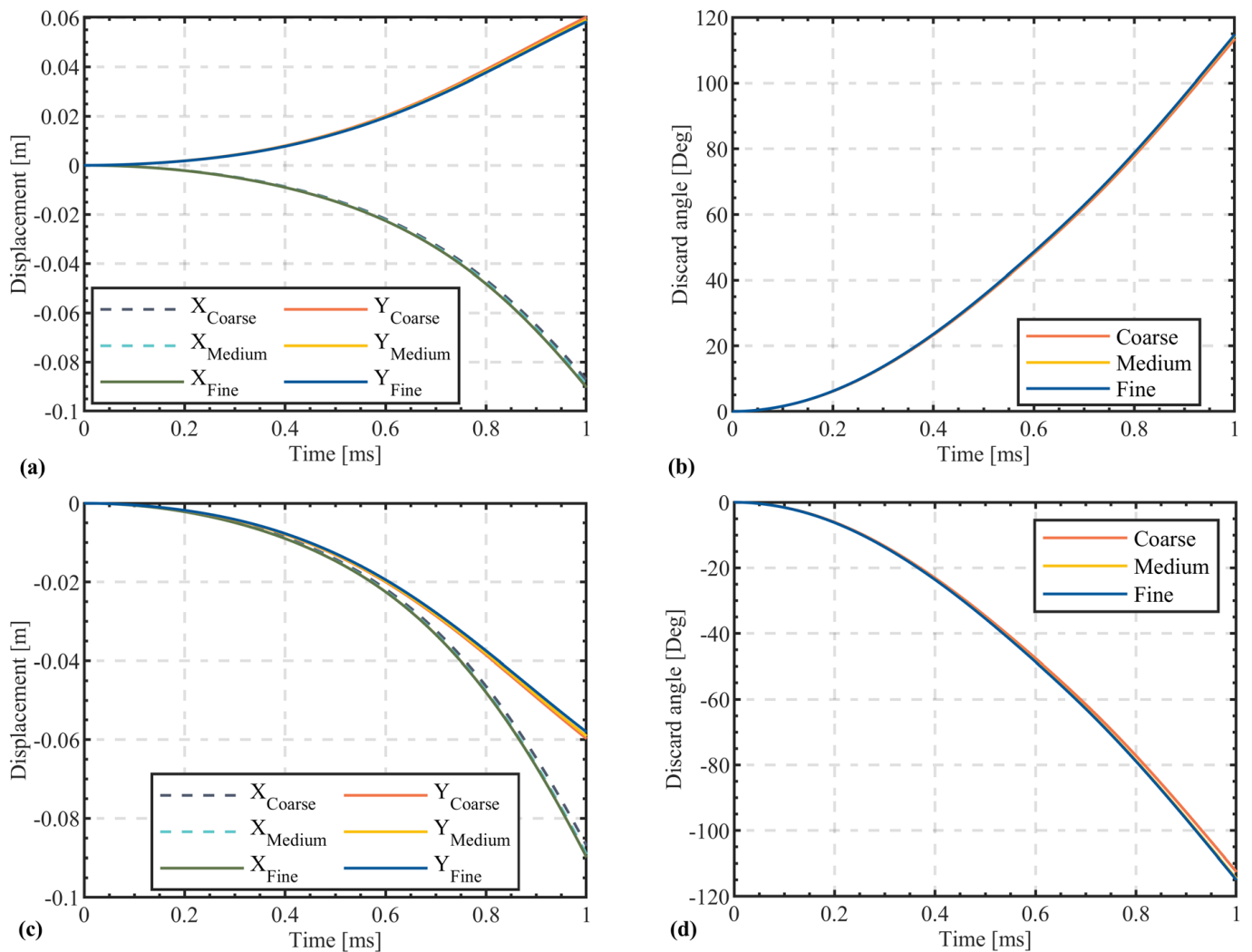


Figure 6. Discard trajectories of the sabot at the AOA = 0 Deg under three sets of grids with different scales in unsteady case: (a) the upper sabot segment's displacement; (b) the upper sabot segment's discard angle; (c) the lower sabot segment's displacement; and (d) the lower sabot segment's discard angle.

4. Results

4.1. Analysis of the Steady Case

Figure 7 illustrates the pressure contours of the flow field for Case 1. The incoming flow generates a detached shock wave at the nose of the flight body. Due to the relatively small obtuse angle of the body, the distance to the detached shock wave is relatively short. At AOAs $\neq 0$ Deg, the flow field around the body shows obvious asymmetry. The lower side of the body experiences an increase in pressure due to the direct impact of the airflow, whereas the upper side, oriented downwind, experiences a decrease in pressure. As the AOA increases, this asymmetry becomes more apparent, with pressure on the lower side rising and pressure on the upper side falling.

The AOA causes significant changes in the pressure distribution on the flight body's surface, as shown in Figure 8. It further affects the aerodynamic forces of the flight body. Figure 9 presents the relationship between the drag and lift coefficients of the body and the AOA. Notably, the lift coefficient exhibits a nearly linear increase with the AOA, while the drag coefficient demonstrates a nonlinear increase.

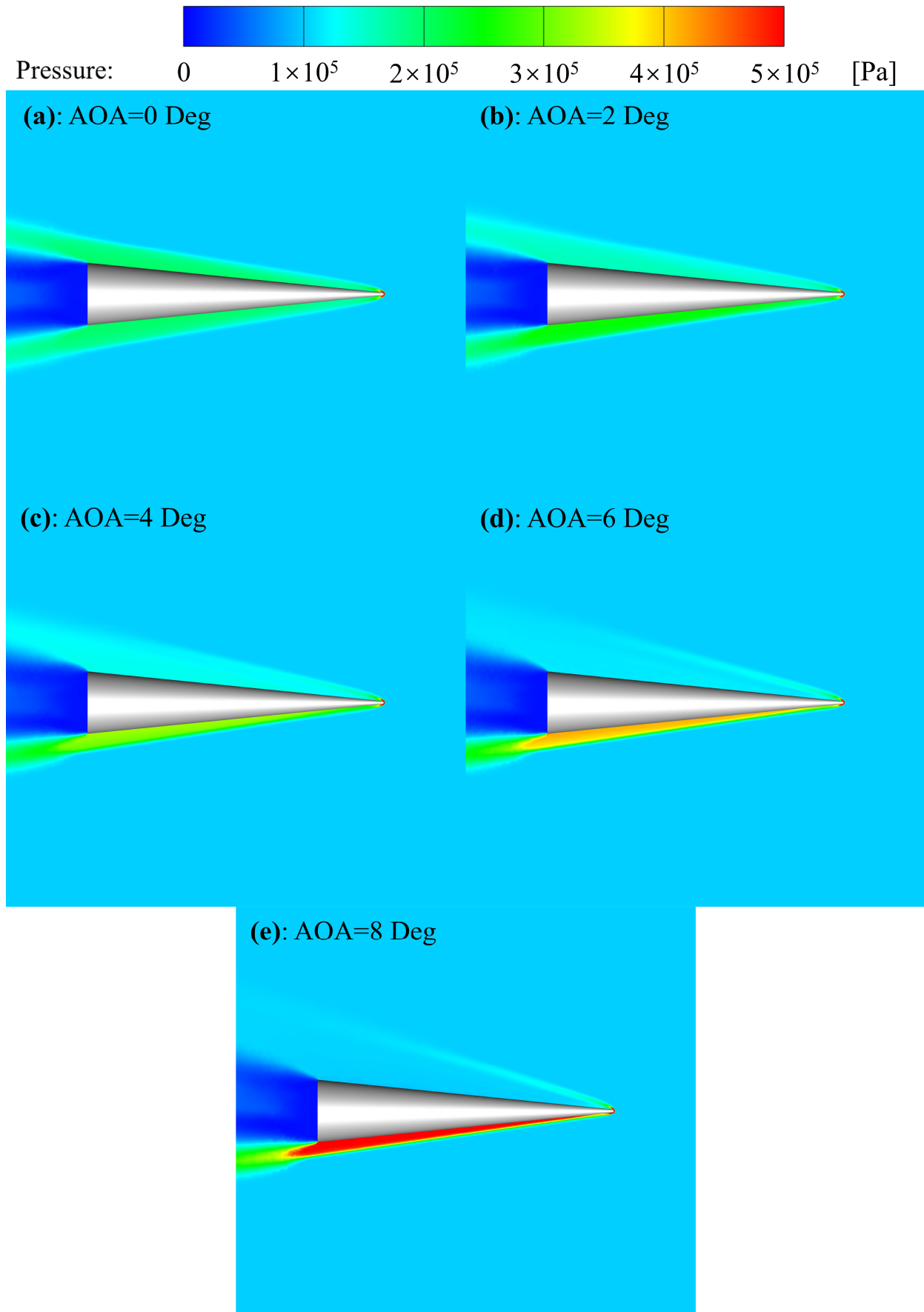


Figure 7. Pressure contour of the flight body: (a) AOA = 0 Deg; (b) AOA = 2 Deg; (c) AOA = 4 Deg; (d) AOA = 6 Deg; and (e) AOA = 8 Deg.

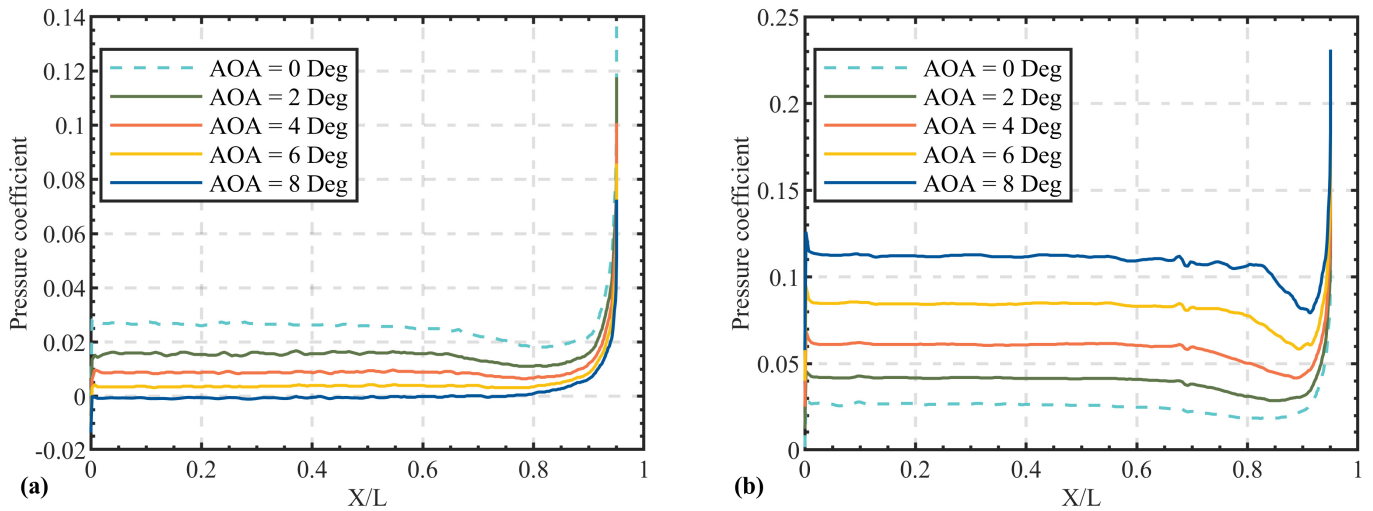


Figure 8. Pressure coefficient of the flight body: (a) upper side; and (b) lower side.

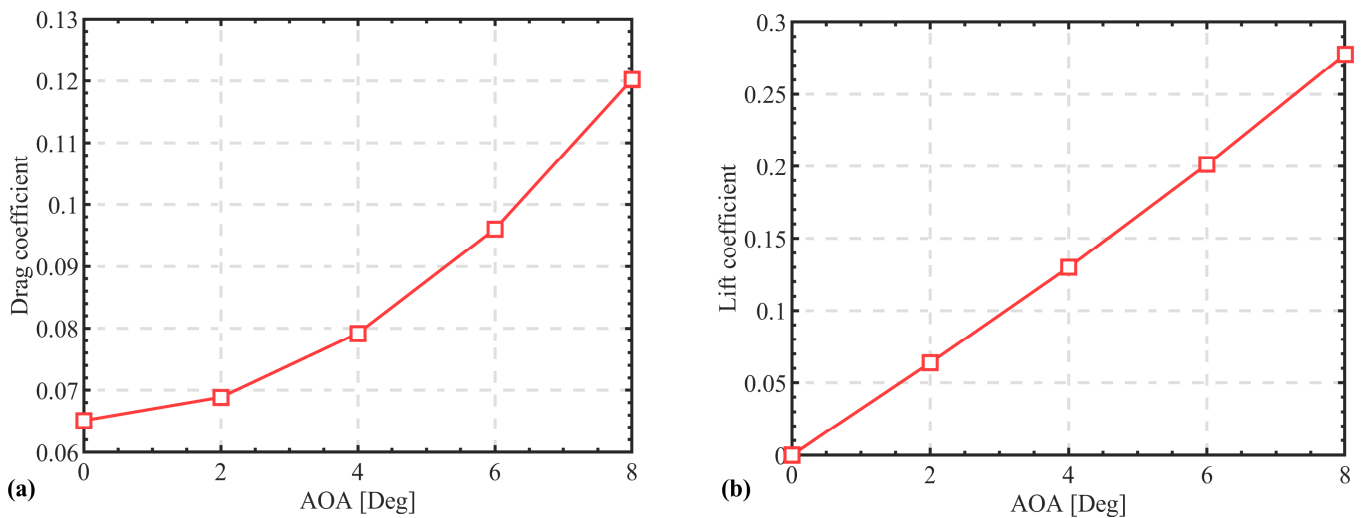


Figure 9. Drag and lift coefficient of the flight body changing with AOA: (a) drag coefficient; and (b) lift coefficient.

Figure 10 shows the flow field pressure contours for Case 2. Affected by the sabot, the flow field of HVP has undergone apparent changes. There is a particular gap between the sabot and the flight body. However, the gap's value is relatively small, resulting in choked flow and creating a high-pressure area in the front cavity of the sabot, which provides force and moment for the sabot discard. At the AOA = 0 Deg, the flow field is symmetric. At AOAs \neq 0 Deg, the flow field is no longer symmetric. The shock wave front on the side facing the incoming flow is pushed further back, making its acting area on the flight body asymmetric. This asymmetry becomes more pronounced as the AOA increases.

Figure 11 presents the relationship between the drag and lift coefficients of the flight body and the AOA under the condition of being equipped with a sabot. Affected by the choked flow, the drag of the flight body increases significantly. At the AOA = 0 Deg, the drag of the flight body increases to 5.24 times that in the state without sabot. If the sabot fails to discard quickly, the flight body's speed will rapidly decay. In addition, when the AOA increases from 0 Deg to 8 Deg, the drag coefficient of the flight body only increases by 6%. This is because when the projectile is in flight with the sabot, the main drag comes from the high-pressure gas induced by the choked flow. However, the AOA significantly affects the lift of the flight body. This is because the AOA causes apparent flow field asymmetry. At the AOA = 8 Deg, the lift coefficient of the flight body increases to 0.05523. However,

due to the obstruction of the sabot, the pressure on the surface of the flight body that is blocked by the sabot is relatively low. Consequently, this lift coefficient is much lower than that in the state without the sabot.

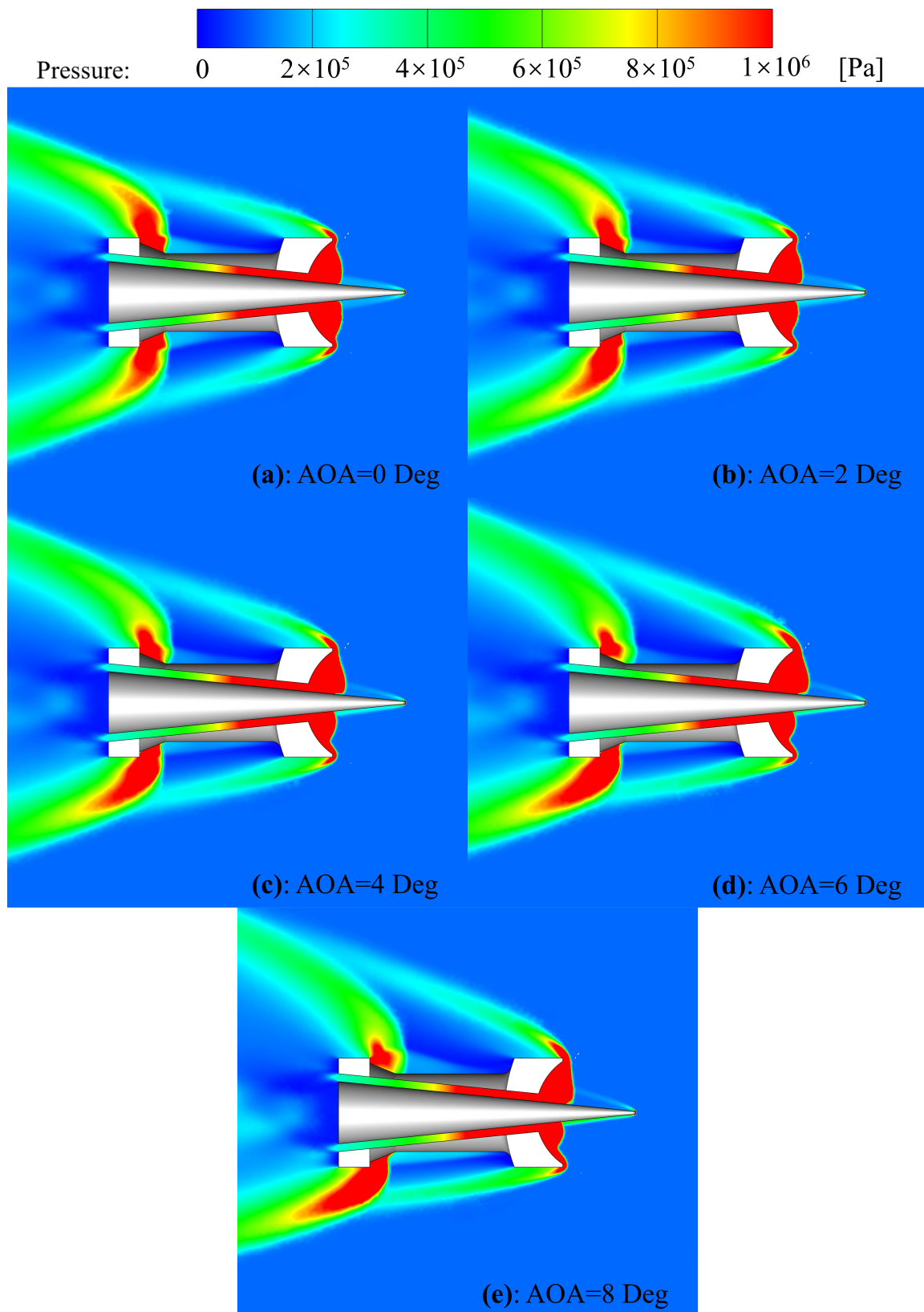


Figure 10. Pressure contour of HVP: (a) AOA = 0 Deg; (b) AOA = 2 Deg; (c) AOA = 4 Deg; (d) AOA = 6 Deg; and (e) AOA = 8 Deg.

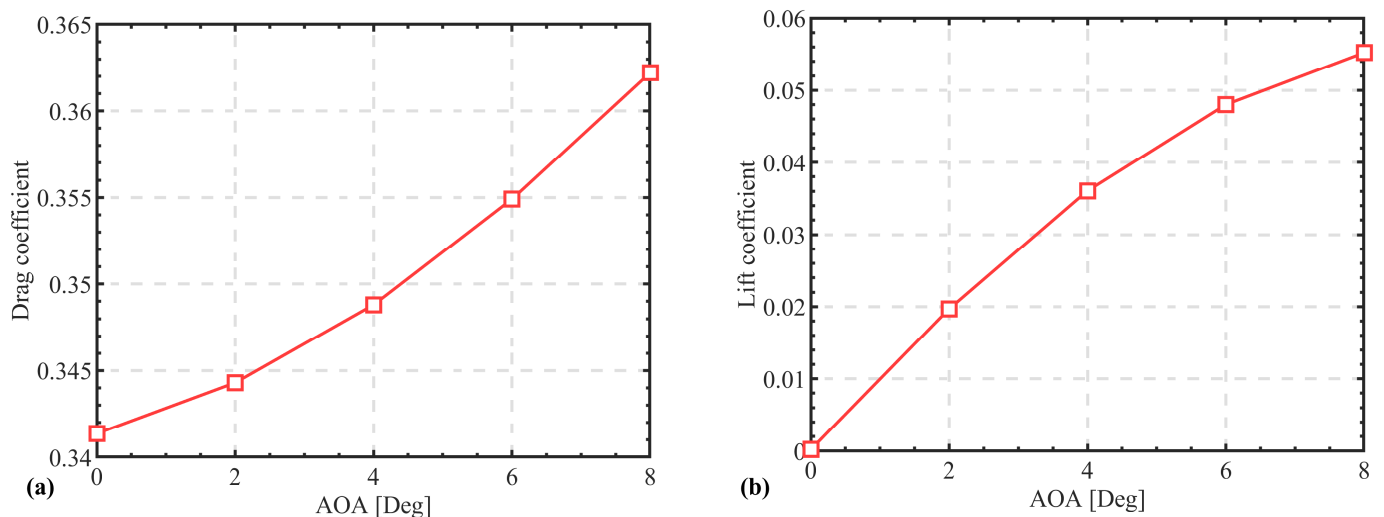


Figure 11. Drag and lift coefficient of the projectile changing with AOA: (a) drag coefficient; and (b) lift coefficient.

The flow field contours and the variations in the flight body's lift and drag coefficients (Figures 10 and 11) show that the sabot seriously affects the flight body's flight. After the projectile exits the barrel's muzzle, if the sabot cannot be discarded quickly, it will rapidly decay the projectile's speed and affect the flight body's attack effectiveness and range.

4.2. Analysis of the Symmetric Discard Flow Field of the Sabot

Figure 12 illustrates the pressure contour of the flow field at different moments under the symmetric discard of the sabot. Figure 13 shows the pressure distribution on the surface of the flight body at different moments.

In the start stage of sabot discard, the gap between the sabot and the flight body is relatively small. The incoming flow captured by the front cavity of the sabot cannot flow through this gap, which leads to choked flow. The formation of the choked flow causes a high-pressure area to be generated in the front cavity of the sabot. This high-pressure area will act on the corresponding positions on the surface of the flight body, as shown in Figure 12a,b, as well as the pressure distribution at $t = 0$ ms and $t = 0.2$ ms in Figure 13.

With discarding, the gap between the flight body and the sabot increases, and the choked flow induced by the sabot and the flight body disappears. Meanwhile, the bow shock wave generated by the sabot begins interacting with the flight body and becomes reflected. Although the gap has increased, their positions are still close, when the reflected shock wave moves towards the tail of the flight body, it will act on the inner wall surface of the sabot and be reflected again. Eventually, the reflected shock wave collides multiple times on the sabot's inner wall surface and the flight body's surface, increasing the pressure on the corresponding collision surfaces, as shown in Figure 12c with the pressure distribution at $t = 0.4$ ms in Figure 13. Besides the head of the flight body, there are two additional local pressure peaks on the surface of the flight body.

With the gap increasing, the intensity of the reflected shock wave decreases. Eventually, the reflection of the oblique shock wave on the inner surface of the sabot will disappear. The oblique shock wave only acts on the flight body's tail, and the reflected shock wave no longer affects the sabot discard, as shown in Figure 12d with the pressure distribution at $t = 0.6$ ms in Figure 13. When the distance between the sabot and the flight body is large enough, the aerodynamic interference between them disappears, as shown in Figure 12e,f with the pressure distribution at $t = 0.8$ ms and $t = 1$ ms in Figure 13.

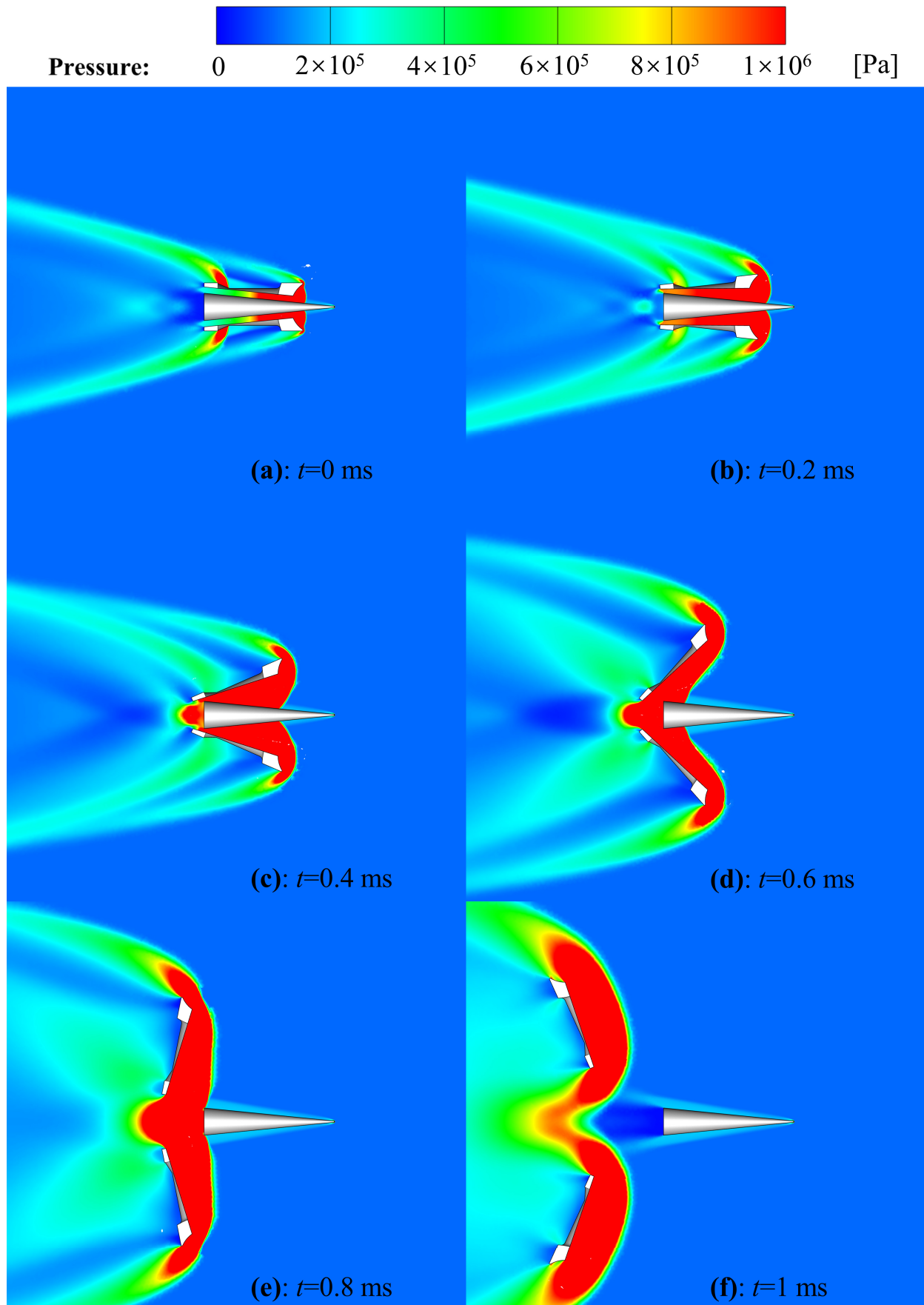


Figure 12. Pressure contour of sabot symmetric discard at different moments: (a) $t = 0$ ms; (b) $t = 0.2$ ms; (c) $t = 0.4$ ms; (d) $t = 0.6$ ms; (e) $t = 0.8$ ms; and (f) $t = 1$ ms.

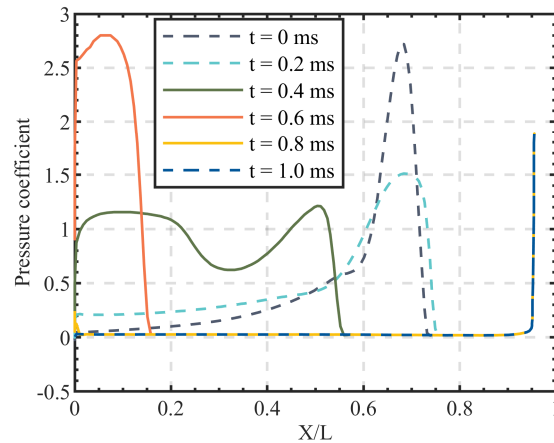


Figure 13. Pressure coefficient distribution of the surface of the flight body at different moments under the sabot symmetric discard.

Figure 14 shows the variation in the flight body's drag coefficient with time during the symmetric sabot discard. The gap between the sabot and the flight body is small in the early stage. As the sabot slightly opens, the high-pressure gas in the front cavity of the sabot moves towards the rear, causing the range of the high-pressure area to increase, as shown in Figure 12a,b with the pressure distribution at $t = 0$ ms and $t = 0.2$ ms in Figure 13. The drag of the flight body tends to increase and reaches a peak at 0.376 ms. At this moment, the drag coefficient is 0.3566, and the discard angle of the upper and lower sabot segments are 20.98 Deg and -20.98 Deg, respectively.

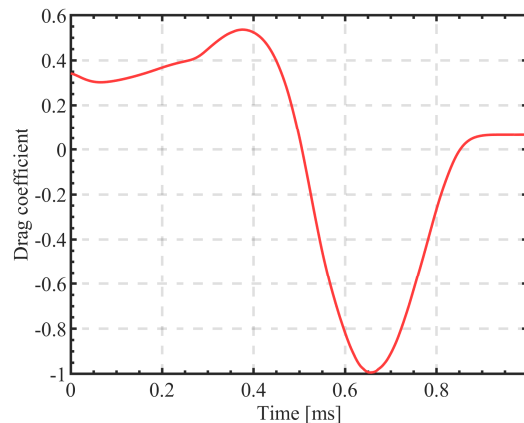


Figure 14. Drag coefficient of the flight body with time under the condition of the sabot symmetric discard.

As the absolute value of the discard angle (AVODA) increases, the gap between the sabot and the flight body gradually increases. The high-pressure gas in the front part of the flight body flows to the rear. It forms a high-pressure area at the flight body's tail, which then leads to a rapid decrease in the drag of the flight body, as shown in Figure 12c,d with the pressure distribution at $t = 0.4$ ms and $t = 0.6$ ms in Figure 13. The drag turns into thrust, and the drag coefficient becomes negative. At $t = 0.655$ ms, the drag coefficient reaches the reverse peak value of -0.9938 , and the discard angle of the upper and lower sabot segments are 56.11 Deg and -56.11 Deg, respectively. After that, as the sabot gradually moves away from the flight body, the distance between the high-pressure area formed by the sabot and the base of the flight body also gradually increases, which then leads to a rapid increase in the drag again, as shown in Figure 12e,f with the pressure distribution at $t = 0.8$ ms and $t = 1$ ms in Figure 13.

As the distance between the sabot and the flight body becomes larger and larger, the influence of the sabot's flow field on the flight body's flow field gradually weakens, and the

drag coefficient becomes stable. At $t = 1$ ms, the drag coefficient returns to 0.06566, equal to the value calculated in Case 1. This indicates that the subsequent flight of the flight body will no longer be disturbed by the sabot's flow field.

During the symmetric discard of the sabot, the flight body's drag coefficient fluctuates significantly within a short period, which does not contribute to its flight stability.

The discard trajectories of the sabot are shown in Figure 15. The X-direction displacements of the upper and lower sabot segments have coincided with each other, and the Y-direction displacements of the upper and lower sabot segments are symmetric, with a calculation error of less than 0.14%. The discard angles of the upper and lower sabot segments are symmetric. The AVODA is 114.5 Deg, and the calculation error is less than 0.2%.

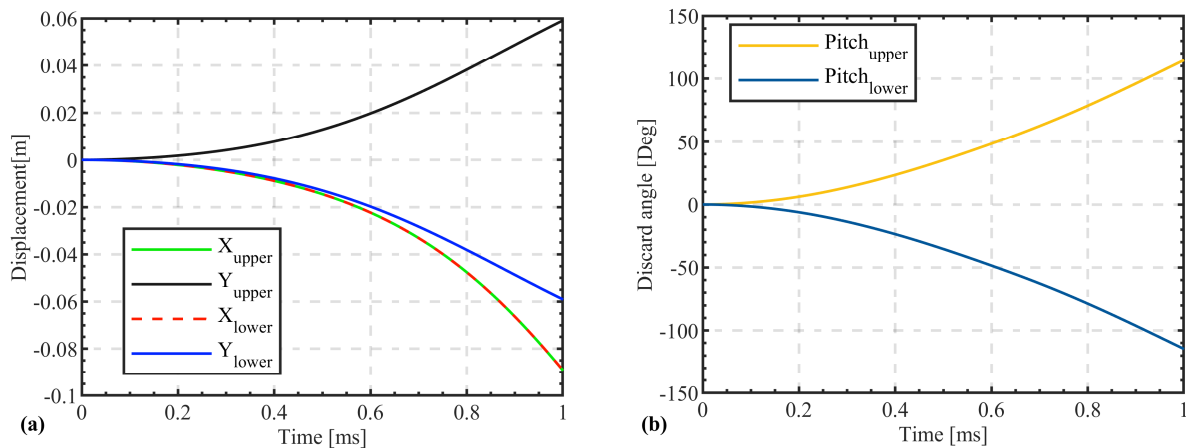


Figure 15. Discard trajectories: (a) displacement; and (b) discard angles.

4.3. Analysis of the Asymmetric Discard Flow Field of the Sabot

The pressure distribution on the upper and lower sabot segment changes at AOAs $\neq 0$ Deg, as shown in Figure 16. The high-pressure part represents the sabot's inner wall, while the relatively low-pressure part represents the back-side wall. As the AOA increases, the difference between the upper and lower sabot segments becomes more significant, mainly reflected in the high-pressure area in the sabot's front cavity and on the sabot's back side, increasing the asymmetry of the discard.

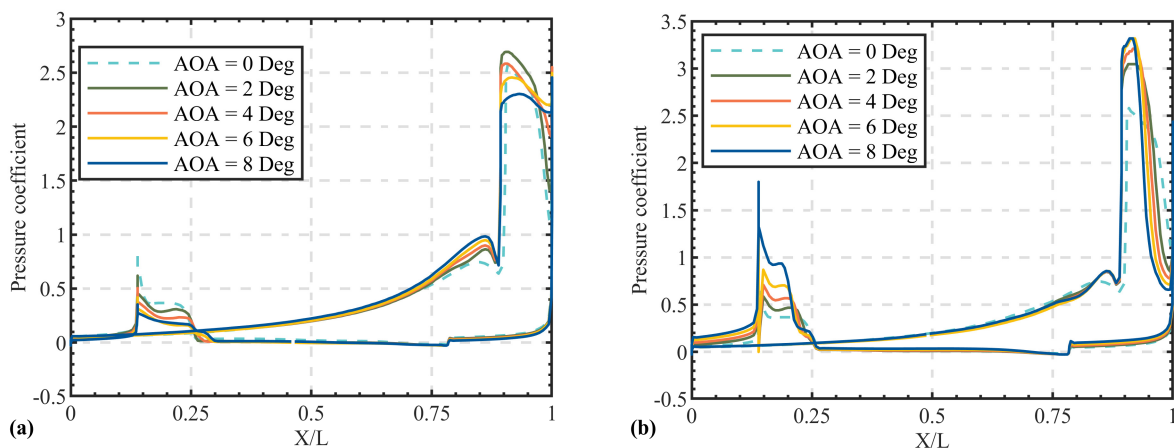


Figure 16. Pressure distribution on the surface of the sabot at different AOAs and $t = 0$ ms: (a) the upper sabot segment; and (b) the lower sabot segment.

Figures 17–20 illustrate the contours of the flow field at different moments under the condition of the asymmetric sabot discard. The influences of the upper and lower sabot segments on the flight body are no longer the same during asymmetric sabot discard.

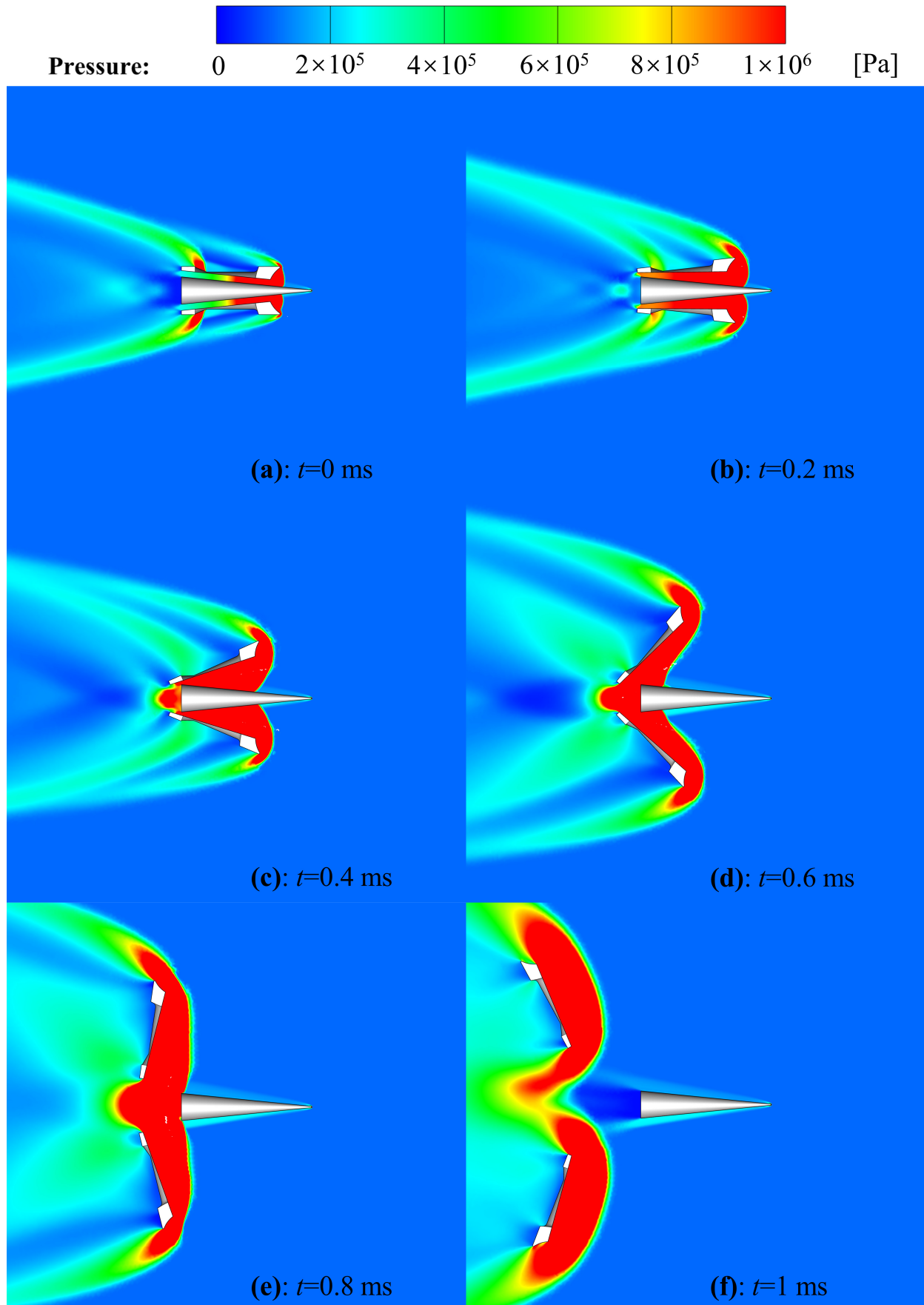


Figure 17. Pressure contour of the flow field of the sabot asymmetric discard at AOA = 2 Deg: (a) $t = 0$ ms; (b) $t = 0.2$ ms; (c) $t = 0.4$ ms; (d) $t = 0.6$ ms; (e) $t = 0.8$ ms; and (f) $t = 1$ ms.

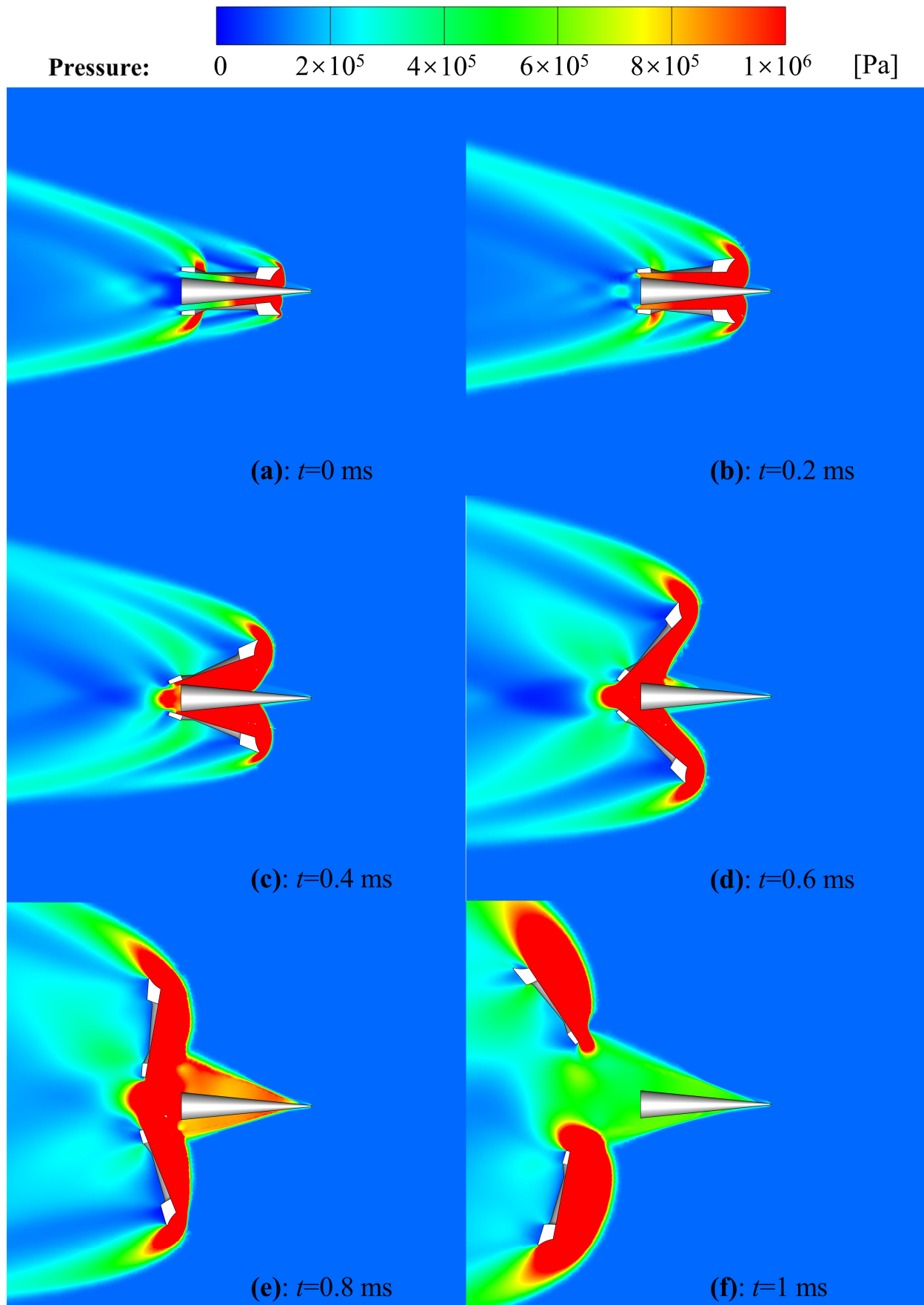


Figure 18. Pressure contour of the flow field of the sabot asymmetric discard at AOA = 4 Deg: (a) $t = 0$ ms; (b) $t = 0.2$ ms; (c) $t = 0.4$ ms; (d) $t = 0.6$ ms; (e) $t = 0.8$ ms; and (f) $t = 1$ ms.

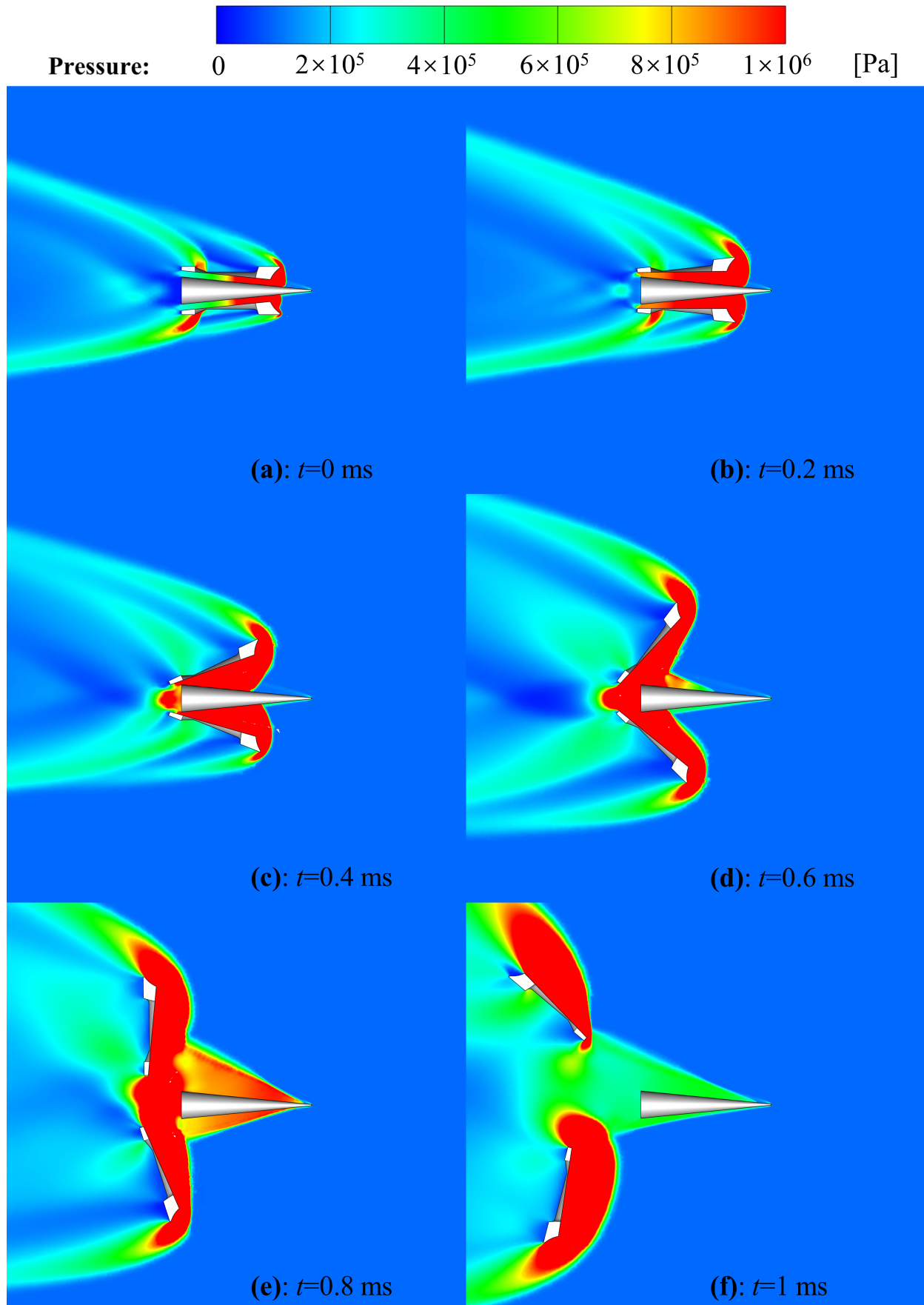


Figure 19. Pressure contour of the flow field of the sabot asymmetric discard at AOA = 6 Deg: (a) $t = 0$ ms; (b) $t = 0.2$ ms; (c) $t = 0.4$ ms; (d) $t = 0.6$ ms; (e) $t = 0.8$ ms; and (f) $t = 1$ ms.

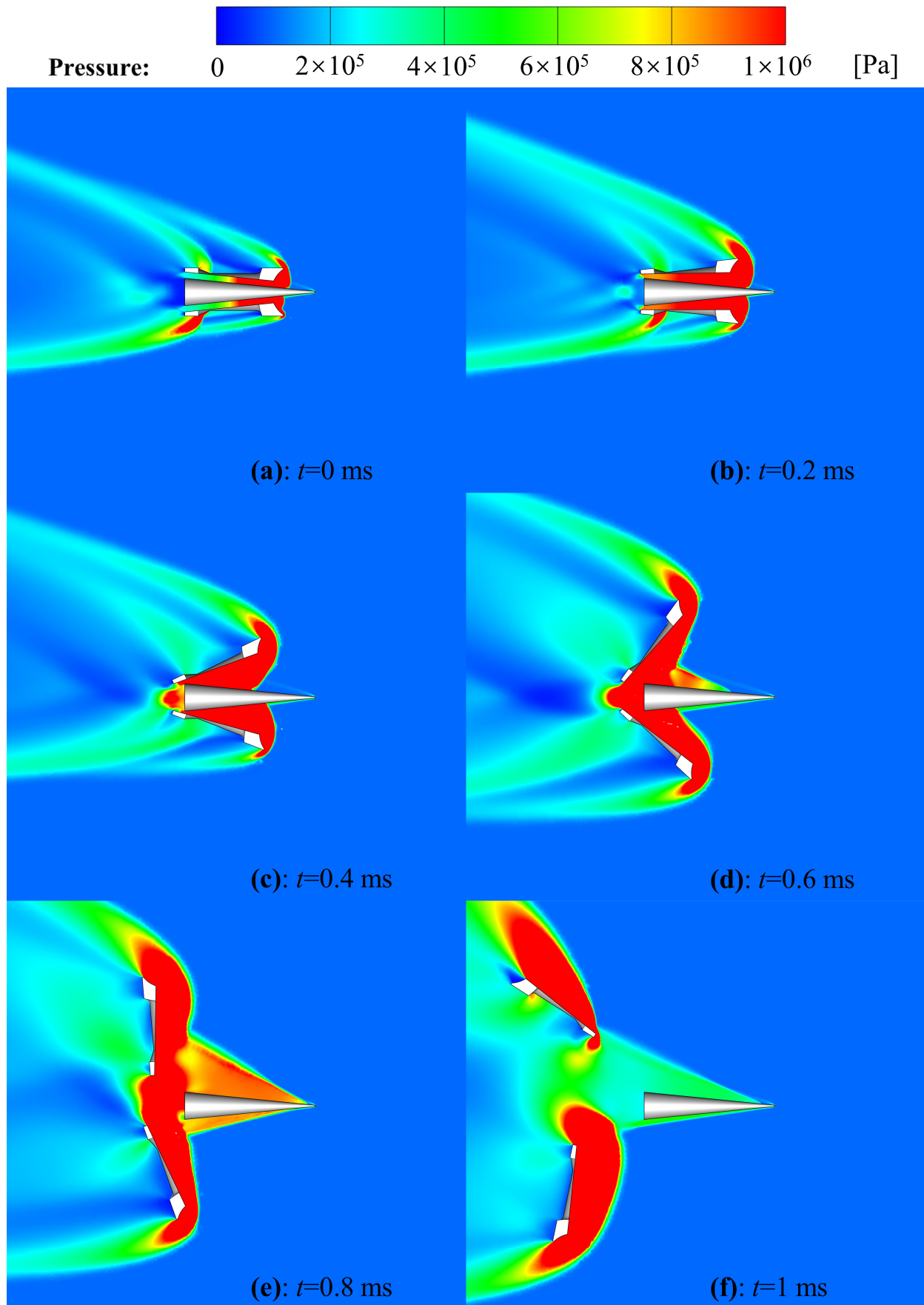


Figure 20. Pressure contour of the flow field of the sabot asymmetric discard at AOA = 8 Deg: (a) $t = 0$ ms; (b) $t = 0.2$ ms; (c) $t = 0.4$ ms; (d) $t = 0.6$ ms; (e) $t = 0.8$ ms; and (f) $t = 1$ ms.

At the $AOA = 2$ Deg, the change in the direction of the incoming flow is relatively small, and the asymmetry of the sabot discard is insignificant. Therefore, the flow field results are like those under the symmetric. However, during the sabot discard at $AOAs = 4, 6,$ and 8 Deg, affected by factors such as the direction of the incoming flow, the asymmetry of discard, and the change in the discard speed of the sabot, choking occurs at the tail of the flight body. The gas in the high-pressure area at the tail expands and diffuses towards the head, causing high-pressure gas to reattach to the surface of the flight body, thereby prolonging the time during which the flight body is disturbed, as shown in (d), (e), and (f) of Figures 18–20. Moreover, as the AOA increases, the disturbance from the sabot becomes more evident and more persistent.

The variations in the lift and drag coefficient of the flight body with time during the sabot discard process at different $AOAs$ are shown in Figure 21. The drag coefficient curves almost overlap in the early stage of the sabot discard before the drag is transformed into thrust. However, after the drag is transformed into thrust, there are apparent differences in the drag changes in the flight body at different $AOAs$. Regarding the thrust of the flight body, as the AOA increases, the peak value and duration of the thrust decrease. The lift change in the flight body is pronounced because of the changed direction of the incoming flow and the asymmetry of discard. The peak value of the lift coefficient increases with the increase in the AOA . It can be observed from the changes in the drag and lift of the flight body that the asymmetric discard of the sabot causes an evident disturbance to the flight body. The disturbance is more apparent with the increase in the asymmetry.

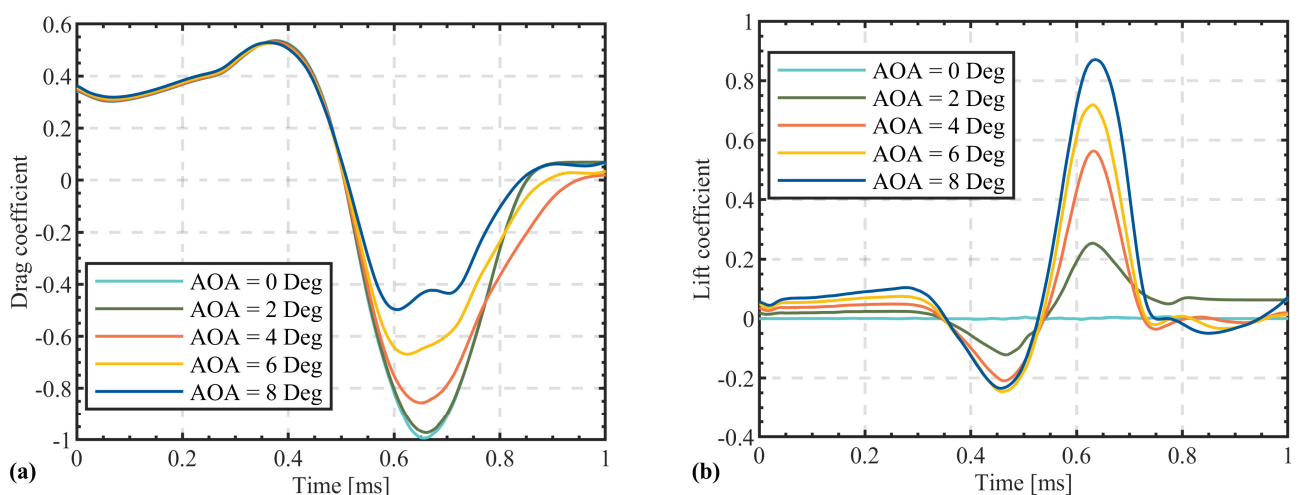


Figure 21. Drag and lift coefficients of the flight body with time under the condition of asymmetric discard of sabot: (a) drag coefficients; and (b) lift coefficients.

It can be seen from the variations in the drag and lift coefficient that there are differences in the changes in the lift and drag at the $AOA = 2$ Deg compared with those at $AOAs = 4, 6,$ and 8 Deg. This is because the flow field at the $AOA = 2$ Deg differs from that at $AOAs = 4, 6,$ and 8 Deg. In the latter three, there is a situation where the high-pressure gas expands and diffuses along the flight body, as illustrated in Figures 18d, 19d and 20d.

Considering the differences in the sabot discard flow fields under the $AOAs = 2, 4, 6,$ and 8 Deg, a further discussion on the sabot discard disturbance at $AOAs = 2$ and 4 Deg was carried out. Figure 22 shows the pressure distribution on the surface of the flight body at the two $AOAs$ and different moments. At the $AOA = 2$ Deg, a relatively slight asymmetry appears in the pressure distribution on the flight body's upper and lower side walls. The pressure distribution curves at 0.8 ms and 1 ms almost coincide, like the pressure distribution shown in Figure 13. At the $AOA = 4$ Deg, a relatively significant asymmetry appears in the pressure distribution on the flight body's upper and lower side

walls. There are also apparent differences in the pressure distribution at $t = 0.8$ ms and $t = 1$ ms, caused by the high-pressure gas expanding from the tail to the nose of the flight body. At the AOA = 2 Deg and $t = 1$ ms, the drag coefficient recovers to 0.06928, which is only 0.6% different from 0.06885 in Case 1. The lift coefficient recovers to 0.06284, only 1.5% different from 0.06379 in Case 1. However, at the AOA = 4 Deg and $t = 1$ ms, the lift and drag coefficients differ quite a lot from those in Case 1. The time of calculation at the AOA = 4 Deg is extended in this study. It is observed that the lift and drag coefficients return to the steady state at $t = 1.4$ ms. Compared with the discard at the AOA = 2 Deg, the recovery time is extended by 40%.

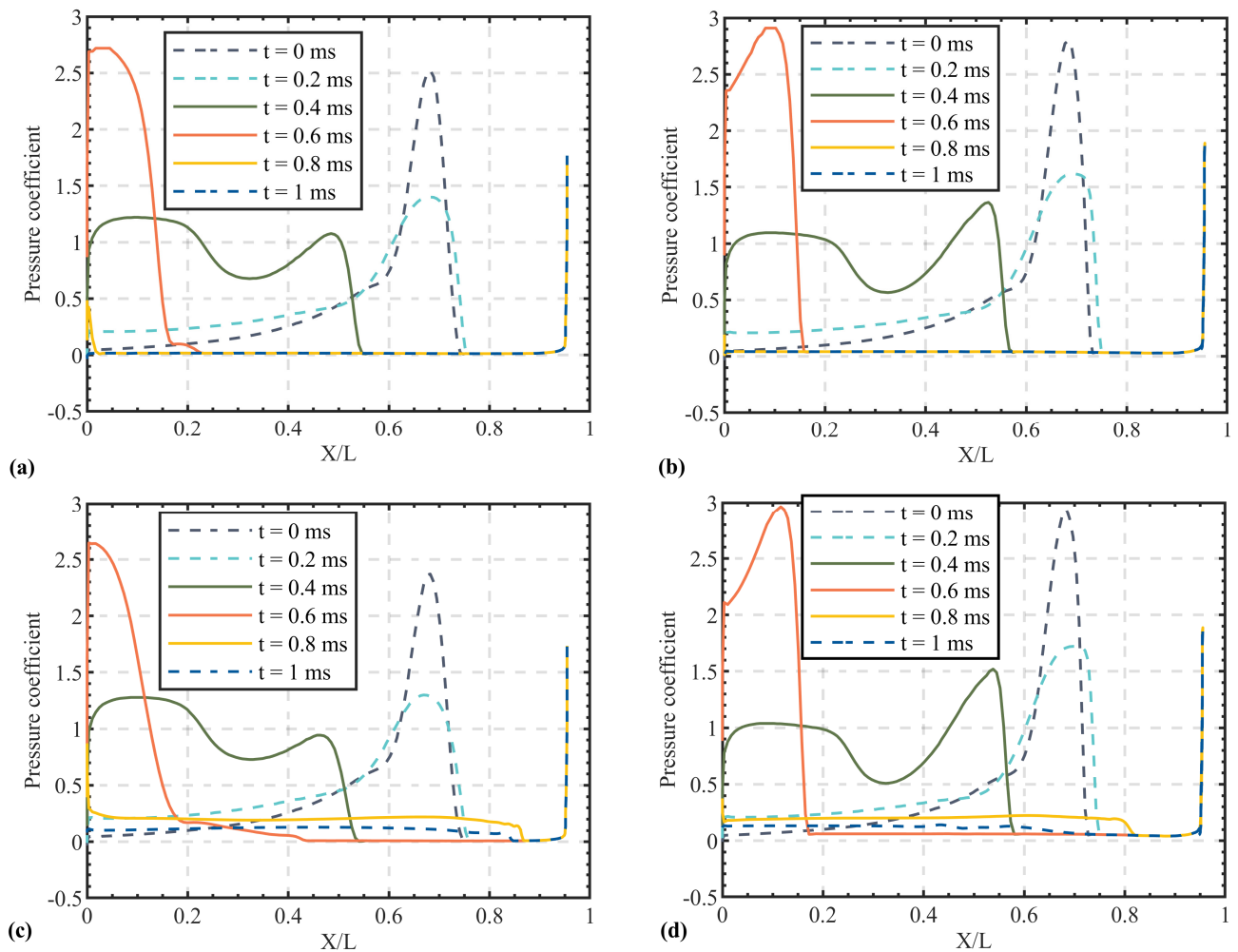


Figure 22. Pressure coefficient distribution of the surface of the flight body under the AOA = 2 Deg and AOA = 4 Deg: (a) upper side of the flight body at AOA = 2 Deg; (b) lower side of the flight body at AOA = 2 Deg; (c) upper side of the flight body at AOA = 4 Deg; and (d) lower side of the flight body at AOA = 4 Deg.

Figure 23 shows the sabot discard trajectories at different AOAs. At the AOA = 8 Deg, the X-direction displacement of the upper sabot segment only changes by 1.2 mm, and the Y-direction displacement only changes by 3.3 mm, with a deviation of less than 3.3%. It can be considered that the change in the AOA has almost no impact on the displacement of the upper sabot segment. For the lower sabot segment, the X-direction displacement changes by 8.2 mm, and the Y-direction displacement changes by 9.8 mm, with a deviation of 11.9%. The change in the AOA has a particular impact on the displacement of the lower sabot segment. As the AOA increases, the X- and Y-direction displacements of the lower sabot segment both decrease. The influence of the AOA is mainly reflected in the discard

angles. The AVODAs of the upper and lower sabot segments are 114.5 Deg at the AOA = 0. However, the upper sabot segment accelerates while the lower sabot segment decelerates at AOAs \neq 0 Deg. Notably, at the AOA = 8 Deg, the AVODA of the upper sabot segment increases to 147 Deg, increasing by 28%. The AVODA of the lower sabot segment decreases to 102 Deg, decreasing by 10.9%. At $t = 1$ ms, the difference in AVODA of the upper and lower sabot segments reaches 45 Deg.

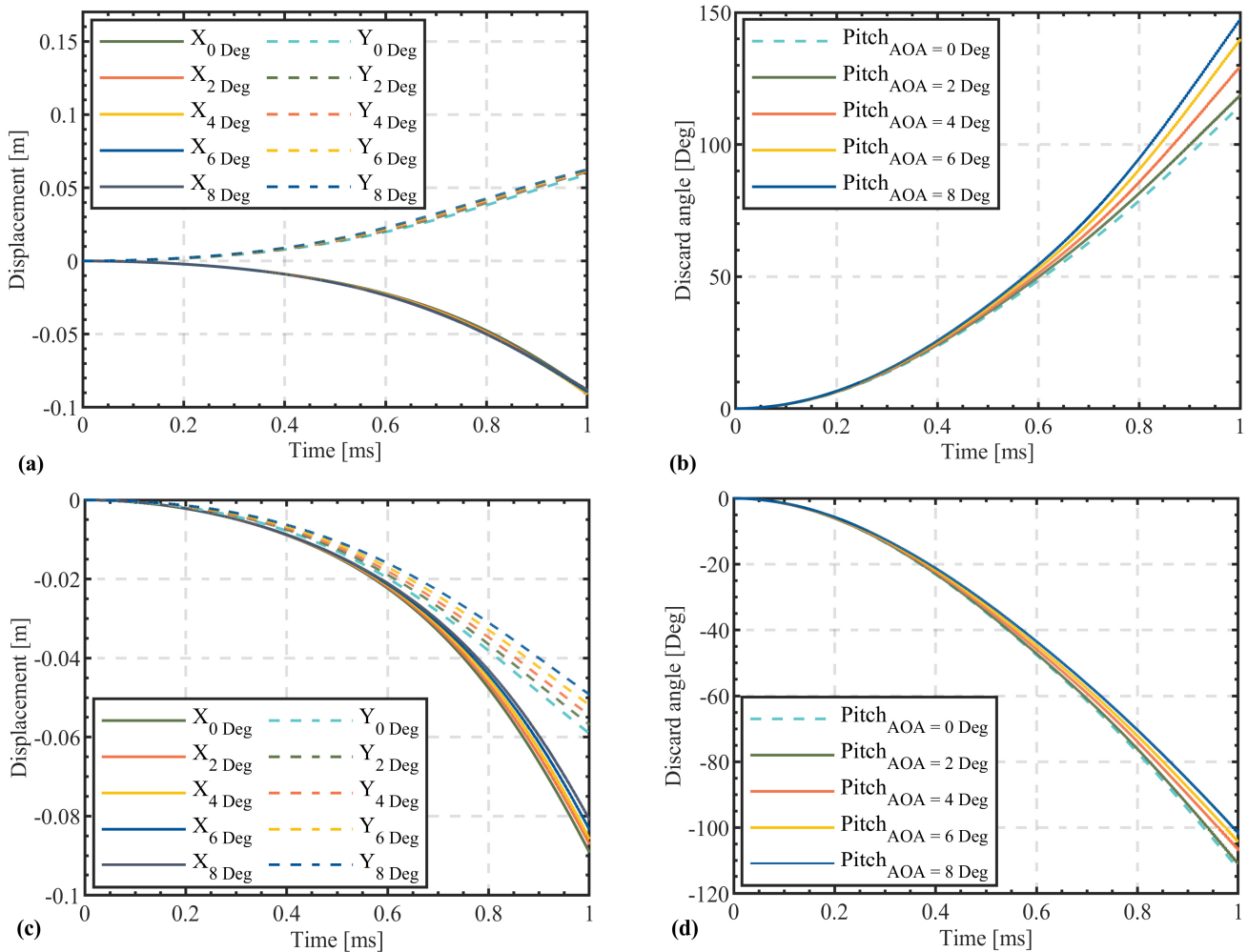


Figure 23. Discard trajectories at different AOAs: (a) displacement of the upper sabot segment; (b) discard angles of the upper sabot segment; (c) displacement of the lower sabot segment; and (d) discard angles of the lower sabot segment.

At the AOA = 2 Deg, the lift and drag coefficients of the flight body return to the steady state within 1 ms. Moreover, compared with the symmetric discard, the deviations of the discard angles of the upper and lower sabot segments are 4% and 3%, respectively, and the displacement deviations are below 3%, with all the deviations being lower than 4%. When the AOA only increases to 4 Deg, the recovery time of the lift and drag coefficients is extended by 40%, the deviations of the discard angles of the upper and lower sabot segments increase to 12% and 6.5%, respectively, and the displacement deviations increase to more than 5%. Considering that in the actual launches, the projectile cannot be at the AOA = 0 Deg after exiting the muzzle. To avoid excessive disturbances caused by the asymmetric sabot discard, the acceptable AOA range for the sabot discard of HVP is from -2 Deg to 2 Deg.

5. Discussion and Conclusions

The study focuses on the problem of sabot discard for HVP at Mach 7.2 with upper and lower sabot segments. The unstructured overset grid method, the Realizable $k - \epsilon$ turbulence model, and the 3DOF motion model are adopted to conduct the sabot discard flow field numerical calculations. The influence of the AOA is discussed and analyzed. The main conclusions obtained are as follows:

1. At AOAs $\neq 0$ Deg, the steady flow field of the flight body is no longer symmetric. The pressure on the lower surface of the flight body increases while the pressure on the upper decreases. Moreover, the lift coefficient exhibits a linear increase with the AOA, while the drag coefficient demonstrates a nonlinear increase.
2. Affected by the sabot, significant changes occur in the flow field. A high-pressure area is generated in the sabot's front cavity, and the flight body's drag increases to 5.24 times that in the steady state. At AOAs $\neq 0$ Deg, the flow field is no longer symmetric, and the shock wave surface on the side facing the incoming flow is pushed further back. The phenomenon that the sabot induces a significant increase in the drag of the flight body is also observed in HVPs with varying geometric configurations. The sabots of HVPs typically have a front-cavity structure, which can result in a choking phenomenon. Consequently, a high-pressure area is formed in the front cavity of the sabot, which directly leads to a significant increase in the drag coefficient of the flight body. This phenomenon serves as a valuable reference for sabot design and optimization, highlighting the necessity for designers to implement strategies aimed at minimizing both the mass and the moment of inertia of the sabot. Such measures are essential to facilitate prompt sabot discard, thereby preventing prolonged interference with the flight body. Failure to address these considerations may result in a substantial increase in drag, which could lead to a rapid decline in the kinetic energy of the flight body. Furthermore, the high-pressure gas in the front cavity of the sabot generates the aerodynamic force and moment necessary for the sabot discard. To ensure the reliability of this discard process, it is imperative for designers to focus on the front-cavity structure.
3. During the sabot discard, in the early stage of the discard, the small gap between the sabot and the flight body leads to choking. As the gap widens, the choking disappears, and the sabot shock wave acts on the flight body and reflects between the flight body's surface and the sabot. When the sabot moves away from the flight body, the shock wave no longer reflects, and the oblique shock wave of the sabot only acts on the tail of the flight body. During the sabot discard, the drag coefficient fluctuates significantly. The sabot shock wave generates a high-pressure area at the tail of the flight body. The high-pressure area causes the drag coefficient to drop from 0.3566 to -0.9938 , turning the drag into thrust. As the sabot moves away, the drag coefficient recovers from -0.9938 to 0.06566. The phenomenon of drag fluctuation is also observed in the sabot discard of other HVPs. This occurrence is attributed to the close relationship between the location of the high-pressure region and the position of the flight body. During the sabot discard process, the sabot retreats in relation to the flight body, resulting in the high-pressure gas acting at a position that shifts toward the base of the flight body. Consequently, this movement contributes to a reduction in the drag experienced by the flight body. Once the sabot has sufficiently distanced itself from the flight body, the drag of the flight begins to improve.
4. At AOAs $\neq 0$ Deg, the sabot discard is asymmetric. The upper sabot segment accelerates while the lower sabot segment decelerates. As the AOA increases, the asymmetry becomes more evident. At the AOA = 8 Deg, the difference in the AVODAs of the upper and lower sabot segments increases to 45 Deg. During the asymmetric discard,

the aerodynamic interference between the sabot and the flight body becomes more complicated. When the AOA exceeds 4 Deg, there is a situation where the high-pressure area at the tail of the flight body expands towards the nose, which prolongs the duration of the disturbance by more than 40%. Therefore, to avoid the influence of the discard disturbance on the flight stability of the flight body, it is recommended that the AOA for HVP sabot discard be maintained within a range of -2 to 2 Deg. In practical applications, the range of AOAs imposes certain requirements on the launch barrel and control system. The launch barrel needs to maintain good straightness and avoid excessive wear. Regular maintenance and timely repair of the barrel should be considered to ensure that the barrel is in good condition. Regarding the control system, it is advisable to implement dynamic compensation mechanisms to mitigate external disturbances. By combining real-time environmental data—such as wind direction and platform vibrations—and historical test results, the control system can adjust the launch angle accordingly to counteract the effects of external disturbances, thereby ensuring that the AOA remains within the recommended range.

One limitation that should be noted is the absence of direct experimental–numerical comparisons through image-based validation. Images of the sabot discard were not captured in the relevant experiment [22]. Nevertheless, this study presents a comprehensive overview of essential parameters for simulation, including the model’s geometry, grid, boundary conditions, and time step. These parameters ensure the reproducibility of the numerical simulation. The numerical method is validated using the WPFS standard benchmark, and various grid configurations are employed to assess grid independence. These approaches enhanced the reliability of the simulation results despite the lack of experimental image correlation.

Future investigation will employ the proposed numerical method to systematically investigate the sabot discard of HVP across a range of variables, including size, geometry, material, environment, and velocity. The findings derived from these calculations will facilitate the quantification of the relationships between the discard trajectories—specifically, the distance and AOA—and time under different conditions. This analysis aims to clarify the characteristics of sabot discard across varying scenarios. Additionally, dimensional normalization will be applied to derive universally applicable principles of sabot discard.

Author Contributions: Conceptualization, X.Y. and J.L.; methodology, X.Y. and J.L.; software, X.Y. and Z.X.; validation, X.Y. and Z.X.; formal analysis, X.Y., S.T. and B.L.; investigation, X.Y., J.L. and S.T.; resources, J.L. and S.T.; data curation, X.Y. and B.L.; writing—original draft preparation, X.Y.; writing—review and editing, X.Y. and J.L.; visualization, X.Y., B.L. and Z.X.; supervision, J.L. and B.L.; project administration, J.L.; funding acquisition, J.L. and B.L. All authors have read and agreed to the published version of the manuscript.

Funding: This research was funded by the National Natural Science Foundation of China (No. 92266301, No. 92166204, and No. 52207071).

Data Availability Statement: The data that support the findings of this study are available from the corresponding author upon reasonable request.

Acknowledgments: We acknowledge the data resources from the “National Space Science Data Center, National Science & Technology Infrastructure of China. (<https://www.nssdc.ac.cn>, accessed on 21 January 2025)”. We acknowledge the data provider Computational Aerodynamics Institute of China Aerodynamics Research and Development Center.

Conflicts of Interest: The authors declare no conflicts of interest.

Abbreviations

The following abbreviations are used in this manuscript:

HVP	Hypervelocity Projectile
SSGG	Single-stage gas guns
SSPG	Single-stage power guns
2SLGG	Two-stage light gas guns
3SLGG	Three-stage light gas guns
VDF	Van de Graaff accelerators
LDF	Laser-driven flyers
LIPIT	Laser-induced particle impact tests
APFSDS	Fin-stabilized discarding sabot armor-piercing projectile
6DOF	Six-degree-of-freedom
3DOF	Three-degree-of-freedom
CFD	Computational fluid dynamics
FVM	Finite volume method
WPFS	Wing-pylon-finned-Store
AVODA	Absolute value of the discard angle

References

- Rogers, J.A.; Bass, N.T.; Wiest, M.L.; Wantz, Z.; Wilkerson, J.W.; Lacy, T.E., Jr. The pursuit of hypervelocities: A review of two-stage light gas gun aeroballistic ranges. *Int. J. Impact Eng.* **2024**, *185*, 104861. [[CrossRef](#)]
- Veyssset, D.; Lee, J.H.; Hassani, M.; Kooi, S.E.; Thomas, E.L.; Nelson, K.A. High-velocity micro-projectile impact testing. *Appl. Phys. Rev.* **2021**, *8*, 011319. [[CrossRef](#)]
- Ma, W.; Lu, J.; Liu, Y. Research progress and challenges of electromagnetic launch technology. *Trans. China Electrotech. Soc.* **2023**, *38*, 3943–3959. [[CrossRef](#)]
- O'Rourke, R. *Navy Lasers, Railgun, and Gun-Launched Guided Projectile: Background and Issues for Congress*; Congressional Research Service: Washington, DC, USA, 2019.
- Rogers, J.A.; Bass, N.; Mead, P.T.; Mote, A.; Lukasik, G.D.; Intardonato, M.; Harrison, K.; Leaverton, J.D.; Kota, K.R.; Wilkerson, J.W.; et al. The Texas A&M University hypervelocity impact laboratory: A modern aeroballistic range facility. *Rev. Sci. Instrum.* **2022**, *93*, 085106. [[CrossRef](#)] [[PubMed](#)]
- Barilaro, L.; Wylie, M.; Shafeeg, T. Design of the Sabot-Stopping System for a Single-Stage Light-Gas Gun for High-Velocity Impacts. *Appl. Sci.* **2023**, *13*, 7664. [[CrossRef](#)]
- Stilp, A.J. Sabot designs for launching penetrators and projectiles. In *High-Pressure Shock Compression of Solids VIII: The Science and Technology of High-Velocity Impact*; Chhabildas, L.C., Davison, L., Horie, Y., Eds.; Springer: Berlin, Germany, 2005; pp. 201–225. ISBN 3-540-22866-7.
- Ma, W.; Lu, J.; Li, X. Electromagnetic launch hypervelocity integrated projectile. *J. Natl. Univ. Def. Technol.* **2019**, *41*, 1–10. [[CrossRef](#)]
- Schmidt, E.; Shear, D. Aerodynamic interference during sabot discard. *J. Spacecr. Rocket.* **1978**, *15*, 162–167. [[CrossRef](#)]
- Song, W.; Ai, B. Multibody separation dynamics: Review. *Acta Aeronaut. Astronaut. Sin.* **2022**, *43*, 25950. [[CrossRef](#)]
- Charlton, E.; Davis, M. Computational optimization of the F-35 external fuel tank for store separation. In Proceedings of the 46th AIAA Aerospace Sciences Meeting and Exhibit, Reno, NV, USA, 7–10 January 2008; p. 376. [[CrossRef](#)]
- Wang, Y.; Wang, Y.; Jiang, Z. Numerical investigation of aerodynamic separation schemes for two-stage-to-orbit-like two-body system. *Aerosp. Sci. Technol.* **2022**, *131*, 107995. [[CrossRef](#)]
- Cui, P.; Jia, H.; Chen, J.; Zhou, G.; Wu, X.; Ma, M.; Li, H.; Tang, J. Numerical Investigation on Unsteady Shock Wave/Vortex/Turbulent Boundary Layer Interactions of a Hypersonic Vehicle during Its Shroud Separation. *Aerospace* **2022**, *9*, 619. [[CrossRef](#)]
- Song, W.; Ai, B. Research progress on multibody aerodynamics. *Chin. J. Theor. Appl. Mech.* **2022**, *54*, 1461–1484. [[CrossRef](#)]
- Schmidt, E.M. Wind-Tunnel Measurements of Sabot-Discard Aerodynamics. *J. Spacecr. Rocket.* **1981**, *18*, 235–240. [[CrossRef](#)]
- Li, H.; Cui, D.; He, Z.; Guo, J.; Guan, X.; Liu, D. Visualization of Flight Attitude of a Fin-stabilized Sabot Discard Projectile Near the Muzzle. *Acta Armamentarii* **1992**, *13*, 66–69.
- Zielinski, A.E.; Weinacht, P.; Bennett, J. Electromagnetic and aeromechanical analysis of sabot discard for railgun projectiles. *J. Spacecr. Rocket.* **2000**, *37*, 257–264. [[CrossRef](#)]

18. Huang, Z.; Wessam, M.E.; Chen, Z. Numerical investigation of the three-dimensional dynamic process of sabot discard. *J. Mech. Sci. Technol.* **2014**, *28*, 2637–2649. [[CrossRef](#)]
19. Li, X.; Lu, J.; Feng, J.; Du, P.; Wu, X. Simulation model for sabot discard using dynamic mesh technique. *J. Natl. Univ. Def. Technol.* **2018**, *40*, 9–13. [[CrossRef](#)]
20. Reck, B.; Hundertmark, S.; Simicic, D.; Hruschka, R.; Sauerwein, B.; Leopold, F.; Schneider, M. Behavior of a railgun launch package at the muzzle and during sabot discard. *IEEE Trans. Plasma Sci.* **2019**, *47*, 2545–2549. [[CrossRef](#)]
21. Mohanan, S.; Rajesh, G. Trajectory predictions of new lift separation sabots. *Def. Technol.* **2021**, *17*, 1361–1373. [[CrossRef](#)]
22. Kasahara, H.; Matsuo, A. Three-dimensional numerical investigation of hypersonic projectile launched by railgun on transitional ballistics. *J. Spacecr. Rocket.* **2021**, *58*, 919–935. [[CrossRef](#)]
23. Kharlamov, D.; Zeiner, A.; Martinez, B. Investigation of the Impact of the Sabot-Discard on the Trajectory of a Kinetic Energy Projectile. In Proceedings of the AIAA AVIATION 2023 Forum, San Diego, CA, USA, 12–16 June 2023; p. 3714. [[CrossRef](#)]
24. You, G. Launch disturbances of armor-piercing fin-stabilized discarding sabot projectile. *J. Ballist.* **1991**, *04*, 45–54.
25. Liu, F.; Song, Y.; Yu, H.; Lin, W.; Zhang, J.; Si, Z.; Ding, M.; Rui, X. Study on the influence of projectile on muzzle disturbance. *Def. Technol.* **2018**, *14*, 570–577. [[CrossRef](#)]
26. Huang, Z.; Xia, C.; Cao, Y.; Chen, Z.; Zhang, H. Numerical investigations on the sabots discard process of an APFSDS at different angles of attack. *Weily J. Eng.* **2019**, *2019*, 373–378. [[CrossRef](#)]
27. Bi, H.; Wang, Z.; Wang, H.; Zhou, Y. Aerodynamic phenomena and drag of a maglev train running dynamically in a vacuum tube. *Phys. Fluids* **2022**, *34*, 096111. [[CrossRef](#)]
28. Shih, T.H.; Liou, W.W.; Shabbir, A.; Yang, Z.; Zhu, J. *A New K-Epsilon Eddy Viscosity Model for High Reynolds Number Turbulent Flows: Model Development and Validation*; NASA-TM-106721; NASA. Lewis Research Center: Cleveland, OH, USA, 1994.
29. Erengil, M.E. An Aerodynamic Method for Symmetric Sabot Separation. In Proceedings of the 37th AIAA Aerospace Sciences Meeting and Exhibit, Reno, NV, USA, 11–14 January 1999. [[CrossRef](#)]
30. Kasahara, H.; Matsuo, A. Three-dimensional Shock Wave Interactions in Sabot Separation Launched in Hypersonic Regime. *Jpn. Soc. Aeronaut. Space Sci.* **2022**, *65*, 147–159. [[CrossRef](#)]
31. Chen, J.; Wu, X.; Zhang, J.; Li, B.; Jia, H.; Zhou, N. FlowStar: General unstructured-grid CFD software for National Numerical Wind tunnel (NNW) Project. *Acta Aeronaut. Astronaut. Sin.* **2021**, *42*, 625739. [[CrossRef](#)]
32. Tian, S.; Fu, J.; Chen, J. A numerical method for multi-body separation with collisions. *Aerosp. Sci. Technol.* **2021**, *109*, 106426. [[CrossRef](#)]
33. Li, S.; Ning, X.; Luo, X.; Hou, Z.; Bo, J. Aerodynamic interference characteristics of near-ground multibody separation by electromagnetic launch. *Acta Aeronaut. Astronaut. Sin.* **2024**, *45*, 129884. [[CrossRef](#)]
34. Heim, E.R. *CFD Wing/Pylon/Finned Store Mutual Interference Wind Tunnel Experiment*; Arnold Engineering Development Center, Air Force Systems Command, United States Air Force: Tullahoma, TN, USA, 1991.
35. Computational Aerodynamics Institute of China Aerodynamics Research and Development Center. Verification and Validation Calibration Model Database. 1.0. National Space Science Data Center. Available online: https://vssso.nssdc.ac.cn/nssdc_en/html/vsssoinfo.html?1400 (accessed on 20 January 2025).
36. Chen, B.; Luo, L.; Jiang, A.; Wu, X.; Zhang, P.; Jia, H. Numerical simulation of separation characteristics for internally buried weapon at high Mach number. *J. Beijing Univ. Aeronaut. Astronaut.* **2024**, *50*, 2113–2122. [[CrossRef](#)]
37. Yan, X.; Niu, J.; Xu, Y.; Li, C. Numerical Research on Store Separation Based on Polyhedral Overset Mesh. *Phys. Gases* **2024**, *9*, 36–44. [[CrossRef](#)]
38. Tang, Z.; Li, B.; Zhemg, M.; Deng, Y. Store separation simulation using overset unstructured grid. *Acta Aerodyn. Sin.* **2009**, *27*, 592–596.
39. Sheharyar, M.; Uddin, E.; Ali, Z.; Zaheer, Q.; Mubashar, A. Simulation of a Standard Store Separated from Generic Wing. *J. Appl. Fluid Mech.* **2018**, *11*, 1579–1589. [[CrossRef](#)]

Disclaimer/Publisher’s Note: The statements, opinions and data contained in all publications are solely those of the individual author(s) and contributor(s) and not of MDPI and/or the editor(s). MDPI and/or the editor(s) disclaim responsibility for any injury to people or property resulting from any ideas, methods, instructions or products referred to in the content.